



ARTICLE

Toward Analytical Homogenized Relaxation Modulus for Fibrous Composite Material with Reduced Order Homogenization Method

Huilin Jia¹, Shanqiao Huang¹ and Zifeng Yuan^{1,2,*}

¹HEDPS, Center for Applied Physics and Technology (CAPT), Department of Mechanics and Engineering Science, Peking University, Beijing, 100871, China

²State Key Laboratory for Turbulence and Complex Systems, Peking University, Beijing, 100871, China

*Corresponding Author: Zifeng Yuan. Email: yuanzifeng@pku.edu.cn

Received: 21 October 2024 Accepted: 04 December 2024 Published: 03 January 2025

ABSTRACT

In this manuscript, we propose an analytical equivalent linear viscoelastic constitutive model for fiber-reinforced composites, bypassing general computational homogenization. The method is based on the reduced-order homogenization (ROH) approach. The ROH method typically involves solving multiple finite element problems under periodic conditions to evaluate elastic strain and eigenstrain influence functions in an ‘off-line’ stage, which offers substantial cost savings compared to direct computational homogenization methods. Due to the unique structure of the fibrous unit cell, “off-line” stage calculation can be eliminated by influence functions obtained analytically. Introducing the standard solid model to the ROH method enables the creation of a comprehensive analytical homogeneous viscoelastic constitutive model. This method treats fibrous composite materials as homogeneous, anisotropic viscoelastic materials, significantly reducing computational time due to its analytical nature. This approach also enables precise determination of a homogenized anisotropic relaxation modulus and accurate capture of various viscoelastic responses under different loading conditions. Three sets of numerical examples, including unit cell tests, three-point beam bending tests, and torsion tests, are given to demonstrate the predictive performance of the homogenized viscoelastic model. Furthermore, the model is validated against experimental measurements, confirming its accuracy and reliability.

KEYWORDS

Homogenized relaxation modulus; viscoelastic; standard solid model; reduced order homogenization; fibrous composite material

1 Introduction

Fiber-reinforced composites offer advantages such as lightweight properties, high strength, extended maintenance intervals, and corrosion resistance, making them widely used in the aerospace and automotive industries [1–5]. Thermosetting or thermoplastic matrices with cylindrical microstructures exhibit transversely isotropic viscoelastic behavior, as documented in the literature [6,7]. The overall mechanical behavior of fibrous composites is analyzed using multiscale methods. These



methods provide detailed insights into the underlying mechanisms, enabling material performance optimization and guiding innovative material design.

Initially, homogenization methods for viscoelastic composites were based on the correspondence principle. Micromechanical theoretical schemes developed for elastic composites were extended to viscoelastic composites to estimate their effective elastic moduli in the Laplace domain. Various approaches, including mean-field homogenization methods [8–10], the asymptotic homogenization method [11–13], the variational principle [14,15], and the sequential linearization approach [16], have been employed to simulate viscoelastic composites. Results obtained in the Laplace domain are then transformed back to the time domain to determine the effective response of the viscoelastic materials. However, performing an analytical inverse transform is usually too complex, so the macroscopic response in the time domain can only be obtained through numerical inversion [12] or approximate inversion methods [17], which can be costly and less accurate.

To overcome the limitations of the Laplace transformation, various homogenization methods have been developed to operate directly in the time domain [18–20]. Mean-field homogenization methods, initially formulated for linear elastic composite materials, have since been extended to address nonlinear behaviors, such as elastoplastic [21,22] and viscoelastic [23] responses, among others. These extensions are typically implemented by linearizing local constitutive laws incrementally, an approach necessitated by the Eshelby problem's assumption that mechanical interactions within phases are purely elastic. Additionally, stress and strain fields within each phase are approximated as phase averages, treating them as homogeneous. However, in nonlinear problems, where stress and strain distributions are inherently non-uniform across phases, this approximation can lead to an over-stiffness issue. To address this challenge, techniques such as the isotropization method [24] and higher-order theories [25] have been proposed. Bleiler et al. [26] introduced a tangent second-order homogenization method to estimate the effective mechanical response of fibrous composites with hyperelastic, anisotropic, and incompressible phases. Furthermore, Barral et al. [27] advanced the Mori-Tanaka method by incorporating a modified transformation field analysis (TFA) approach first proposed by Dvorak and his coworkers [28] and introducing a specialized coating between fibers and the matrix, effectively mitigating over-stiffness in the analysis of fiber-reinforced composites. In the TFA method, the inelastic strains are considered as given eigenstrains. This method assumes that eigenstrains in each phase of the composite are piecewise constant, this lower-order approximation can lead to inaccurate solutions for overall properties. To overcome the problem, Michel et al. [29,30] have introduced the nonuniform transformation field analysis, where full field calculations take place and the plastic behavior is traced with the help of several plastic modes. Strategies such as subdividing each phase into numerous partitions, using asymptotically consistent eigenstrain fields have also been employed [31].

The asymptotic homogenization method is a mathematically rigorous methodology developed by Sanchez-Palencia [32], Bensoussan and Alain [33]. Compare to the Mean-field homogenization method, it effectively captures the interactions between different phases within composite materials, enabling more precise predictions of their overall performance. It has been proved that the considered fields converge towards the homogeneous macroscopic solution as the micro-structural parameter $\xi = x/y$ tends to 0. The classic asymptotic homogenization method can obtain the linear homogenized modulus by solving a linear unit cell problem with given phase material elastic properties. Thus, one can use the homogenized elastic properties in a macroscopic simulation without downscaling or upscaling between the macro- and meso-scales. In this manner, the linear homogenization process is named as “off-line” process. However, if material nonlinearities at the mesoscale are considered, a unit cell problem must be solved at every integration point of all the macroscopic elements during

each macroscopic *Newton-Raphson* iteration. Additionally, the unit cell problem itself requires a *Newton-Raphson* iterative process due to material nonlinearities. This repeating process is known as the “on-line” process since it depends on the “on-the-fly” kinematic measurements at the macro-scale, significantly increasing the computational cost. Yu et al. [34] used the asymptotic homogenization method to solve thermo-viscoelastic problems, considering both multiple spatial and temporal scales. Zhai et al. [18] developed a time-domain asymptotic homogenization method based on the integral form of the Kelvin–Voigt viscoelastic model and used it for woven fabric composites.

Multiscale computational techniques based on the finite element method such as FE^2 , offer the possibility of computing the macro-structural response of heterogeneous materials with an arbitrary microscopic geometry and constitutive behavior. A scheme based on the discrete homogenization method are developed to predict the effective mechanical properties of 3D dry textiles [35]. Recently, the isogeometric analysis method (IGA), proposed by Hughes and his coworkers [36,37], has been incorporated into computational homogenization [38–40]. The method aims to unify the representation of geometric models and mesh models by directly employing the spline functions as the shape functions. The errors produced by geometric approximations inherent in conventional finite-element and finite-volume techniques could be greatly reduced because the same model is used for both modeling and analysis. Cylindrically orthotropic [41] and viscoelasticity [42] are considered for fiber-reinforced composites using IGH methods.

To decrease computational costs at the meso-scale without significantly compromising solution accuracy, the reduced-order-homogenization (ROH) multiscale method was developed, combining the asymptotic homogenization method with transformation field analysis (TFA) [43,44]. The ROH method was first used in composite plasticity and failure analysis [43,45], and higher-order ROH methods have been developed for three-scale nonlinear problems [46–49]. In this paper, a two-phase model with the assumption of one partition per phase is employed for fiber-reinforced composites. Due to the unique structure of the fiber-reinforced unit cell, analytical transformation influence functions can be derived. Based on ROH theory, an analytical homogenization constitutive model for unidirectional fibrous composites is proposed, eliminating the need for computational homogenization. As demonstrated in the following section, the proposed model does not exhibit significant over-stiffness and helps reduce computational time.

This paper is organized as follows. In [Section 2](#), we introduce the analytical viscoelastic fibrous composites constitutive model based on the ROH homogenization method. Special cases where the fiber volume fraction approaches zero are considered to confirm the model’s consistency under extreme conditions. We investigate the impact of material parameters of each component on the relaxation times of the homogenized viscoelastic material. Additionally, numerical implementation specifics for the proposed model are detailed in this section. [Section 3](#) presents numerical verifications of the proposed model through three sets of numerical examples: unit cell tests, three-point beam bending tests, and torsion tests. Experimental results from the literature are used to validate the proposed constitutive model. Conclusions are provided in [Section 4](#).

2 Methodology

In this section, we introduce an analytical framework to determine homogenized viscoelastic material properties for the fibrous composite material based on the so-called reduced order homogenization (ROH) method. Here we assume the fiber phase follows transversely isotropic symmetry and keeps elastic that

$$\sigma_{ij}^f = L_{ijkl}^f \varepsilon_{kl}^f \quad (1)$$

On the other hand, the matrix phase is viscoelastic and described by the standard solid model [50], and the stress response is written as the following form:

$$\sigma_{ij}^m = L_{ijkl}^{m,\infty} \varepsilon_{kl}^m + \int_0^t e^{-(t-\eta)/\tau_1} L_{ijkl}^{m,iso} \dot{\varepsilon}_{kl}^m(\eta) d\eta \quad (2)$$

where

$$L_{ijkl}^{m,\infty} = 2\mu^{m,\infty} I_{ijkl}^{dev} + 3\kappa^{m,\infty} I_{ijkl}^{vol}, \quad \mu^{m,\infty} = \frac{E^{m,\infty}}{2(1+\nu_m)}, \quad \kappa^{m,\infty} = \frac{E^{m,\infty}}{3(1-2\nu_m)} \quad (3a)$$

$$L_{ijkl}^{m,iso} = 2\mu_{iso}^m I_{ijkl}^{dev} + 3\kappa_{iso}^m I_{ijkl}^{vol}, \quad \mu_{iso}^m = \frac{E_{iso}^m}{2(1+\nu_m)}, \quad \kappa_{iso}^m = \frac{E_{iso}^m}{3(1-2\nu_m)} \quad (3b)$$

Here $E^{m,\infty}$ is the equilibrium Young's modulus of the matrix phase, and ν_m is the corresponding Poisson's ratio. E_{iso}^m is the isotropic relaxation modulus. Finally, the fourth-order tensors I_{ijkl}^{vol} and I_{ijkl}^{dev} are defined as

$$I_{ijkl}^{vol} = \frac{1}{3} \delta_{ij} \delta_{kl}, \quad I_{ijkl}^{dev} = \frac{1}{2} (\delta_{ik} \delta_{jl} + \delta_{il} \delta_{jk}) - \frac{1}{3} \delta_{ij} \delta_{kl} \quad (4)$$

respectively. Here the quantities associated with the fiber and the matrix phase are marked with superscription E^f and E^m , respectively.

Our goal is to obtain an analytical homogeneous relaxation tensor $R_{ijkl}^c(t)$ that

$$\sigma_{ij}^c = L_{ijkl}^{c,\infty} \varepsilon_{kl}^c + \int_0^t R_{ijkl}^c(t-\eta) \dot{\varepsilon}_{kl}^c(\eta) d\eta = L_{ijkl}^{c,\infty} \varepsilon_{kl}^c + R_{ijkl}^c(t) * \dot{\varepsilon}_{kl}^c(t) \quad (5)$$

based on given material properties of the fiber and the matrix phase without computational homogenization process, where σ_{ij}^c , ε_{ij}^c are the macroscopic stress and strain tensor, respectively, $L_{ijkl}^{c,\infty}$ is homogenized linear elastic stiffness tensor, and $f(t) * g(t)$ denotes the convolution of function $f(t)$ and $g(t)$. Here the macroscopic properties are marked with superscription ε^c .

2.1 Reduced Order Homogenization (ROH) for Fibrous Composite Material

The reduced-order homogenization (ROH) method is based on two key assumptions: 1) It is possible to distinguish between two length scales associated with macroscopic and microscopic phenomena; 2) The microstructure is sufficiently regular to be considered periodic; 3) The material within the same partition maintains a consistent status throughout, which reduces computational costs at the meso-scale. A complete derivation of the ROH method would be too extensive for this section, so we will present only the essential formulas. For a detailed explanation of the methodology, please refer to reference [44]. The fibrous composite material consists of the fiber and matrix phases. We introduce eigenstrains μ_{ij} defined as [44]

$$\mu_{ij} = \varepsilon_{ij} - M_{ijkl} \sigma_{kl} \quad (6)$$

where M_{ijkl} is the elastic compliance tensor. The ROH aims to solve the following system of nonlinear equations [44]:

$$\varepsilon_{ij}^f - P_{ij}^{kl,ff} \mu_{kl}^m - P_{ij}^{kl,ff} \mu_{kl}^f = E_{ij}^{kl,f} \varepsilon_{kl}^c \quad (7a)$$

$$\varepsilon_{ij}^m - P_{ij}^{kl,mm} \mu_{kl}^m - P_{ij}^{kl,mf} \mu_{kl}^f = E_{ij}^{kl,m} \varepsilon_{kl}^c \quad (7b)$$

where $E_{ij}^{kl,f}$ and $E_{ij}^{kl,m}$ are the elastic strain influence functions, $P_{ij}^{kl,fm}$, $P_{ij}^{kl,mm}$, $P_{ij}^{kl,ff}$ and $P_{ij}^{kl,mf}$ are the *eigenstrain influence functions*, and ε_{ij}^c is the macroscopic strain tensor.

Since the fiber phase keeps elastic, we can obtain $\mu_{ij}^f = 0$ directly. The eigenstrains of the matrix phase are given as

$$\begin{aligned}\mu_{ij}^m &= \varepsilon_{ij}^m - M_{ijkl}\sigma_{ij}^m = \varepsilon_{ij}^m - (L_{ijkl}^m)^{-1}\sigma_{kl}^m = \varepsilon_{ij}^m - (L_{ijkl}^{m,\infty})^{-1}\sigma_{kl}^m \\ &= -\psi_m \int_0^t e^{-(t-\eta)/\tau_1} \dot{\varepsilon}_{ij}^m(\eta) d\eta\end{aligned}\quad (8)$$

by the standard solid model defined in Eq. (2), with consideration of material isotropy Eqs. (3a) and (3b), and define $\psi_m \equiv E_{iso}^m/E^{m,\infty}$. Here we define

$$L_{ijkl}^m = L_{ijkl}^{m,\infty}\quad (9)$$

By linear elastic stiffness tensor of the fiber phase and the matrix phase given in Eqs. (1) and (9), respectively, we can first obtain the homogenized elastic stiffness tensor L_{ijkl}^c that

$$L_{ijkl}^c = \underbrace{c^f L_{ijmn}^f E_{mn}^{kl,f}}_{\equiv L_{ijkl}^{cf}} + \underbrace{c^m L_{ijmn}^m E_{mn}^{kl,m}}_{\equiv L_{ijkl}^{cm}}\quad (10)$$

where c^f and $c^m = 1 - c^f$ are the volume fraction for the fiber and the matrix phase, respectively. The macro-scopic averaged stress then is given by volumetric averaging of phase stresses that

$$\sigma_{ij}^c = c^f L_{ijkl}^f \varepsilon_{kl}^f + c^m L_{ijkl}^m \varepsilon_{kl}^m = L_{ijkl}^c \varepsilon_{kl}^c + A_{ijkl}^m \mu_{kl}^m\quad (11)$$

where

$$A_{ijkl}^m = c^f L_{ijst}^f P_{st}^{kl,fm} + c^m L_{ijst}^m (P_{st}^{kl,mm} - I_{stkl})\quad (12)$$

Usually, the fibrous composite material is assumed to satisfy the transversely isotropic symmetry so that the linear elastic stiffness tensor can be written with Hill's constants n^c , l^c , m^c , k^c , and p^c [51], with the fibers aligned along the longitudinal x_1 -axis:

$$\{L_{ijkl}^c\} = \begin{bmatrix} n^c & l^c & l^c & & & \\ l^c & k^c + m^c & k^c - m^c & & & \\ l^c & k^c - m^c & k^c + m^c & & & \\ & & & m^c & & \\ & & & & p^c & \\ & & & & & p^c \end{bmatrix}\quad (13)$$

The fiber phase also is transversely isotropic, where its Hill's constants are written as n^f , l^f , m^f , k^f , and p^f . For fibrous composite material, the following universal connections are satisfied [51]:

$$\frac{k^c - k^f}{l^c - l^f} = \frac{k^c - (\lambda^{m,\infty} + \mu^{m,\infty})}{l^c - \lambda^{m,\infty}} = \frac{l^c - c^f l^f - c^m l^m}{n^c - c^f n^f - c^m n^m} = \frac{k^f - (\lambda^{m,\infty} + \mu^{m,\infty})}{l^f - \lambda^{m,\infty}}\quad (14)$$

where $\lambda^{m,\infty}$ and $\mu^{m,\infty}$ are the Lamé constants of the matrix phase.

2.2 Analytical Influence Functions for Fibrous Composite Material

The elastic strain and eigenstrain influence functions are usually evaluated by solving a number of finite element problems over the given fibrous unit cell [44]. In this manuscript, we aim to provide

an analytical method to evaluate those functions with given linear homogenized stiffness tensor L_{ijkl}^c , which can be estimated by Mori-Tanaka or self-consistent method [51].

First of all, the elastic strain influence functions satisfy the following constraint that [44]

$$c^f E_{ij}^{kl,f} + c^m E_{ij}^{kl,m} = I_{ijkl} \quad (15)$$

One can obtain the elastic strain influence functions by Eqs. (10) and (15) [44]:

$$E_{ij}^{kl,f} = \frac{1}{c^f} (L_{ijmn}^f - L_{ijmn}^m)^{-1} (L_{mnkl}^c - L_{mnkl}^m) \quad (16a)$$

$$E_{ij}^{kl,m} = \frac{1}{c^m} (L_{ijmn}^m - L_{ijmn}^f)^{-1} (L_{mnkl}^c - L_{mnkl}^f) \quad (16b)$$

In other words, for a two-phase unit cell, as long as L_{ijkl}^c is given, the elastic strain influence functions can be obtained directly.

Next, we continue to evaluate the eigenstrain influence functions. Define the following supportive tensors:

$$\left\{ \tilde{E}_{ij}^{pq,f} \right\} \equiv \begin{bmatrix} 1 & 0 & 0 & & & \\ -v_{at}^f & 0 & 0 & & & \\ -v_{at}^f & 0 & 0 & & & \\ & & & 0 & & \\ & & & & 0 & \\ & & & & & 0 \end{bmatrix} \quad (17)$$

and

$$\left\{ \tilde{E}_{ij}^{pq,m} \right\} \equiv \begin{bmatrix} 1 & 0 & 0 & & & \\ c^f v_{at}^f / c^m & f_{22} & 0 & & & \\ c^f v_{at}^f / c^m & 0 & f_{33} & & & \\ & & & f_{23} & & \\ & & & & f_{13} & \\ & & & & & f_{12} \end{bmatrix} \quad (18)$$

with v_{at}^f denoting the Poisson's ratio in longitudinal direction of the fiber phase, and

$$f_{ij} = L_{ijij}^c / L_{ijij}^{cm}, \quad ij = 22, 33, 23, 13, 12, \text{ no summation over repeated indices} \quad (19)$$

where L_{ijij}^{cm} is defined in Eq. (10). Then we obtain the eigenstrain influence functions:

$$P_{ij}^{kl,mm} = I_{ijkl} - E_{ij}^{mm,m} \left(\tilde{E}_{mn}^{kl,m} \right)^{-1}, \quad P_{ij}^{kl,f} = I_{ijkl} - E_{ij}^{kl,m} - P_{ij}^{kl,mm} \quad (20a)$$

$$P_{ij}^{kl,fm} = \left(E_{ij}^{mm,f} - \tilde{E}_{ij}^{mm,f} \right) \left(\tilde{E}_{mn}^{kl,m} \right)^{-1}, \quad P_{ij}^{kl,ff} = I_{ijkl} - E_{ij}^{kl,f} - P_{ij}^{kl,fm} \quad (20b)$$

However, $P_{ij}^{kl,mf}$ and $P_{ij}^{kl,ff}$ are not used since $\mu_{ij}^f = 0$.

Due to the symmetry of fibrous unit cell, one can use only 5 non-zero parameters to define one influence tensor. For the linear strain influence tensors, we have ($E = f, m$)

$$\begin{bmatrix} 1 & 0 & 0 \\ E^{11,22} & E^{22,22} & E^{33,22} \\ E^{11,33} & E^{22,33} & E^{33,33} \\ & & & E^{23,23} \\ & & & & E^{13,13} \\ & & & & & E^{12,12} \end{bmatrix} \Rightarrow \begin{bmatrix} 1 & 0 & 0 \\ E^1 & E^2 & E^3 \\ E^1 & E^3 & E^2 \\ & & & E^4 \\ & & & & E^5 \\ & & & & & E^5 \end{bmatrix} \quad (21)$$

and for the eigenstrain influence tensors, we also have ($E = f, m$)

$$\begin{bmatrix} 1 & 0 & 0 \\ P_{22}^{11,mm} & P_{22}^{22,mm} & P_{22}^{33,mm} \\ P_{33}^{11,mm} & P_{33}^{22,mm} & P_{33}^{33,mm} \\ & & & P_{23}^{23,mm} \\ & & & & P_{13}^{13,mm} \\ & & & & & P_{12}^{12,mm} \end{bmatrix} \Rightarrow \begin{bmatrix} 1 & 0 & 0 \\ P_{11}^{mm} & P_{22}^{mm} & P_{33}^{mm} \\ P_{11}^{mm} & P_{33}^{mm} & P_{22}^{mm} \\ & & & P_{44}^{mm} \\ & & & & P_{55}^{mm} \\ & & & & & P_{55}^{mm} \end{bmatrix} \quad (22)$$

From Eqs. (21) and (22), we can quickly obtain the following results:

$$\varepsilon_{11}^m = \varepsilon_{11}^f = \varepsilon_{11}^c \quad (23)$$

which means the axial strains of the matrix and the fiber phases are the same and equals to the macroscopic axial strain ε_{11}^c .

2.3 Viscoelastic Model for the Fibrous Composite Material

In this section, we propose a homogenized viscoelastic model with the analytical elastic strain and eigenstrain influence functions. Substituting Eqs. (8) into (7b) with $\mu_{ij}^f = 0$ yields

$$\varepsilon_{ij}^m + P_{ij}^{kl,mm} \psi_{mm} \int_0^t e^{-(t-\eta)/\tau_1} \dot{\varepsilon}_{kl}^m(\eta) d\eta = E_{ij}^{kl,m} \varepsilon_{kl}^c, \quad (24)$$

$ij = 22, 33, 23, 13, 12$, summation convention over k, l

where $ij = 11$ is not considered due to Eq. (23). In the rest of this section, we derive system of ordinary differential equations (ODEs) for $\dot{\varepsilon}_{ij}^m$ with $ij = 22, 33, 23, 13, 12$. First, taking the derivative of Eq. (24) with respect to time t yields

$$\dot{\varepsilon}_{ij}^m(t) + P_{ij}^{kl,mm} \psi_{mm} \left[\dot{\varepsilon}_{kl}^m(t) - \frac{1}{\tau_1} \int_0^t e^{-(t-\eta)/\tau_1} \dot{\varepsilon}_{kl}^m(\eta) d\eta \right] = E_{ij}^{kl,m} \dot{\varepsilon}_{kl}^c(t) \quad (25)$$

Thus we obtain

$$P_{ij}^{kl,mm} \psi_{mm} \int_0^t e^{-(t-\eta)/\tau_1} \dot{\varepsilon}_{kl}^m(\eta) d\eta = \tau_1 [I_{ijkl} + \psi_m P_{ij}^{kl,mm}] \dot{\varepsilon}_{kl}^m(t) - \tau_1 E_{ij}^{kl,m} \dot{\varepsilon}_{kl}^c(t) \quad (26)$$

Next, substituting Eqs. (26) into (24) yields

$$\varepsilon_{ij}^m + \tau_1 [I_{ijkl} + \psi_m P_{ij}^{kl,mm}] \dot{\varepsilon}_{kl}^m(t) = E_{ij}^{kl,m} [\varepsilon_{kl}^c + \tau_1 \dot{\varepsilon}_{kl}^c(t)], \quad ij = 22, 33, 23, 13, 12 \quad (27)$$

By solving the system of ordinary differential equations in Eq. (27), we obtain the matrix phase strain ε_{ij}^m , where $ij = 22, 33, 23, 13, 12$. The detailed derivation is provided in Appendix A. The solutions for the normal strains $\varepsilon_{22}^m(t)$ and $\varepsilon_{33}^m(t)$ can be expressed as

$$\begin{aligned}
\varepsilon_{22}^m(t) &= E_1^m \varepsilon_{11}^c(t) + E_2^m \varepsilon_{22}^c(t) + E_3^m \varepsilon_{33}^c(t) + \left[-E_1^m \frac{\tau_2 - \tau_1}{\tau_2} - \frac{\tau_1}{\tau_2} \psi_m P_1^{\text{mm}} \right] e^{-t/\tau_2} * \dot{\varepsilon}_{11}^c(t) \\
&+ \left[-\frac{1}{2} (E_2^m + E_3^m) \frac{\tau_2 - \tau_1}{\tau_2} e^{-t/\tau_2} - \frac{1}{2} (E_2^m - E_3^m) \frac{\tau_3 - \tau_1}{\tau_3} e^{-t/\tau_3} \right] * \dot{\varepsilon}_{22}^c(t) \\
&+ \left[-\frac{1}{2} (E_2^m + E_3^m) \frac{\tau_2 - \tau_1}{\tau_2} e^{-t/\tau_2} + \frac{1}{2} (E_2^m - E_3^m) \frac{\tau_3 - \tau_1}{\tau_3} e^{-t/\tau_3} \right] * \dot{\varepsilon}_{33}^c(t)
\end{aligned} \tag{28a}$$

$$\begin{aligned}
\varepsilon_{33}^m(t) &= E_1^m \varepsilon_{11}^c(t) + E_3^m \varepsilon_{22}^c(t) + E_2^m \varepsilon_{33}^c(t) + \left[-E_1^m \frac{\tau_2 - \tau_1}{\tau_2} - \frac{\tau_1}{\tau_2} \psi_m P_1^{\text{mm}} \right] e^{-t/\tau_2} * \dot{\varepsilon}_{11}^c(t) \\
&+ \left[-\frac{1}{2} (E_2^m + E_3^m) \frac{\tau_2 - \tau_1}{\tau_2} e^{-t/\tau_2} + \frac{1}{2} (E_2^m - E_3^m) \frac{\tau_3 - \tau_1}{\tau_3} e^{-t/\tau_3} \right] * \dot{\varepsilon}_{22}^c(t) \\
&+ \left[-\frac{1}{2} (E_2^m + E_3^m) \frac{\tau_2 - \tau_1}{\tau_2} e^{-t/\tau_2} - \frac{1}{2} (E_2^m - E_3^m) \frac{\tau_3 - \tau_1}{\tau_3} e^{-t/\tau_3} \right] * \dot{\varepsilon}_{33}^c(t)
\end{aligned} \tag{28b}$$

The solutions for the shear strains

$$\varepsilon_{23}^m(t) = E_4^m \varepsilon_{23}^c(t) - \frac{\tau_4 - \tau_1}{\tau_4} E_4^m e^{-t/\tau_4} * \dot{\varepsilon}_{23}^c(t) \tag{29a}$$

$$\varepsilon_{13}^m(t) = E_5^m \varepsilon_{13}^c(t) - \frac{\tau_5 - \tau_1}{\tau_5} E_5^m e^{-t/\tau_5} * \dot{\varepsilon}_{13}^c(t) \tag{29b}$$

$$\varepsilon_{12}^m(t) = E_5^m \varepsilon_{12}^c(t) - \frac{\tau_5 - \tau_1}{\tau_5} E_5^m e^{-t/\tau_5} * \dot{\varepsilon}_{12}^c(t) \tag{29c}$$

respectively. With

$$\tau_2 = \tau_1 (1 + \psi_m P_2^{\text{mm}} + \psi_m P_3^{\text{mm}}), \quad \tau_3 = \tau_1 (1 + \psi_m P_2^{\text{mm}} - \psi_m P_3^{\text{mm}}), \tag{30}$$

$$\tau_4 = \tau_1 (1 + \psi_m P_4^{\text{mm}}), \quad \tau_5 = \tau_1 (1 + \psi_m P_5^{\text{mm}})$$

here $\tau_k, k = 2, 3, 4, 5$ are characteristic relaxation times for the fibrous composite materials.

So far, we are able to find the matrix phase strain ε_{ij}^m by the macroscopic strain ε_{ij}^c and the corresponding strain rate $\dot{\varepsilon}_{ij}^c$. In order to obtain an analytical result for macroscopic stress defined in Eq. (11), we continue to derive the eigenstrain of the matrix phase. For μ_{11}^m , we can directly obtain

$$\mu_{11}^m = -\psi_m \int_0^t e^{-(t-\eta)/\tau_1} \dot{\varepsilon}_{11}^m(\eta) d\eta = -\psi_m \int_0^t e^{-(t-\eta)/\tau_1} \dot{\varepsilon}_{11}^c(\eta) d\eta = -\psi_m e^{-t/\tau_1} * \dot{\varepsilon}_{11}^c(t) \tag{31}$$

by considering Eq. (23). For the rest components, expand Eq. (7b) into

$$\begin{bmatrix} P_2^{\text{mm}} & P_3^{\text{mm}} \\ P_3^{\text{mm}} & P_2^{\text{mm}} \end{bmatrix} \begin{Bmatrix} \mu_{22}^m(t) \\ \mu_{33}^m(t) \end{Bmatrix} = \begin{bmatrix} \varepsilon_{22}^m(t) - E_1^m \varepsilon_{11}^c(t) - E_2^m \varepsilon_{22}^c(t) - E_3^m \varepsilon_{33}^c(t) - P_1^{\text{mm}} \mu_{11}^m \\ \varepsilon_{33}^m(t) - E_1^m \varepsilon_{11}^c(t) - E_3^m \varepsilon_{22}^c(t) - E_2^m \varepsilon_{33}^c(t) - P_1^{\text{mm}} \mu_{11}^m \end{bmatrix} \tag{32a}$$

and

$$P_4^{\text{mm}} \mu_{23}^m(t) = \varepsilon_{23}^m(t) - E_4^m \varepsilon_{23}^c(t) \tag{32b}$$

$$P_5^{\text{mm}} \mu_{13}^m(t) = \varepsilon_{13}^m(t) - E_5^m \varepsilon_{13}^c(t) \tag{32c}$$

$$P_5^{\text{mm}} \mu_{12}^m(t) = \varepsilon_{12}^m(t) - E_5^m \varepsilon_{12}^c(t) \tag{32d}$$

Finally, one can introduce a fourth-order tensor $Y_{ij}^{kl,m}(t)$ to represent the eigenstrain $\mu_{ij}^m(t)$ as the following:

$$\mu_{ij}^m(t) = Y_{ij}^{kl,m}(t) * \dot{\varepsilon}_{kl}^c(t) \quad (33)$$

First, from Eq. (31), we can obtain the components corresponding to μ_{11}^m that

$$Y_{11}^{11,m}(t) = -\psi_m e^{-t/\tau_1} \quad (34)$$

From Eqs. (28a) and (28b), we obtain

$$Y_{22}^{11,m}(t) = Y_{33}^{11,m}(t) = \frac{P_1^{mm} \psi_m}{P_2^{mm} + P_3^{mm}} e^{-t/\tau_1} + \left[-\frac{\tau_2 - \tau_1}{\tau_2} \frac{E_1^m}{P_2^{mm} + P_3^{mm}} - \frac{\tau_1}{\tau_2} \frac{P_1^{mm} \psi_m}{P_2^{mm} + P_3^{mm}} \right] e^{-t/\tau_2} \quad (35a)$$

$$Y_{22}^{22,m}(t) = -\frac{\tau_2 - \tau_1}{\tau_2} \frac{E_2^m + E_3^m}{2(P_2^{mm} + P_3^{mm})} e^{-t/\tau_2} - \frac{\tau_3 - \tau_1}{\tau_3} \frac{E_2^m - E_3^m}{2(P_2^{mm} - P_3^{mm})} e^{-t/\tau_3} \quad (35b)$$

$$Y_{33}^{22,m}(t) = -\frac{\tau_2 - \tau_1}{\tau_2} \frac{E_2^m + E_3^m}{2(P_2^{mm} + P_3^{mm})} e^{-t/\tau_2} + \frac{\tau_3 - \tau_1}{\tau_3} \frac{E_2^m - E_3^m}{2(P_2^{mm} - P_3^{mm})} e^{-t/\tau_3} \quad (35c)$$

$$Y_{22}^{33,m}(t) = Y_{33}^{22,m}(t), Y_{33}^{33,m}(t) = Y_{22}^{22,m}(t) \quad (35d)$$

In addition, from Eq. (29b) and (29c), we obtain

$$Y_{23}^{23,m}(t) = -\frac{\tau_4 - \tau_1}{\tau_4} \frac{E_4^m}{P_4^{mm}} e^{-t/\tau_4}, Y_{13}^{13,m}(t) = Y_{12}^{12,m}(t) = -\frac{\tau_5 - \tau_1}{\tau_5} \frac{E_5^m}{P_5^{mm}} e^{-t/\tau_5} \quad (35e)$$

and all other components of Y_{ij}^{kl} are zero. In summary, the components of the eigenstrain $\mu_{ij}^m(t)$ are written as the following:

$$\begin{aligned} \mu_{11}^m(t) &= Y_{11}^{11,m}(t) * \dot{\varepsilon}_{11}^c(t) \\ \mu_{22}^m(t) &= Y_{22}^{11,m}(t) * \dot{\varepsilon}_{11}^c(t) + Y_{22}^{22,m}(t) * \dot{\varepsilon}_{22}^c(t) + Y_{22}^{33,m}(t) * \dot{\varepsilon}_{33}^c(t) \\ \mu_{33}^m(t) &= Y_{33}^{11,m}(t) * \dot{\varepsilon}_{11}^c(t) + Y_{33}^{22,m}(t) * \dot{\varepsilon}_{22}^c(t) + Y_{33}^{33,m}(t) * \dot{\varepsilon}_{33}^c(t) \\ \mu_{23}^m(t) &= Y_{23}^{23,m}(t) * \dot{\varepsilon}_{23}^c(t) \\ \mu_{13}^m(t) &= Y_{13}^{13,m}(t) * \dot{\varepsilon}_{13}^c(t) \\ \mu_{12}^m(t) &= Y_{12}^{12,m}(t) * \dot{\varepsilon}_{12}^c(t) \end{aligned} \quad (36)$$

Substituting Eqs. (33) into (11) yields

$$\sigma_{ij}^c = L_{ijkl}^c \varepsilon_{kl}^c + \underbrace{A_{ijmn}^m Y_{mn}^{kl,m}(t)}_{R_{ijkl}^c(t)} * \dot{\varepsilon}_{kl}^c(t) \quad (37)$$

2.4 Model Consistency in an Extreme Case

In this section, we exam the homogenized viscoelastic properties of the fibrous composite material by letting $c^f = 0$ and $c^m = 1$. Under this situation, the homogenized viscoelastic properties should approach the viscoelastic response of pure matrix phase as well.

By setting $c^m = 1$, one obtains $L_{ijkl}^c = L_{ijkl}^{cm} = L_{ijkl}^m$ through Eq. (10) and $E_{ij}^{kl,m} = I_{ijkl}$. In addition, we have $A_{ijkl}^m = -L_{ijkl}^m$ by Eq. (12). The value of $E_{ij}^{kl,f}$ does not have any meaning. Similarly, by Eq. (18), we obtain $\tilde{E}_{ij}^{pq,m} = I_{ijkl}$ and thus leads to $P_{ij}^{kl,mm} = 0$ by Eq. (20a). This result guarantees that $\tau_k = \tau_1$, $k = 2, 3, 4, 5$ by Eq. (30).

Considering the aforementioned conditions, we can obtain $\varepsilon_{ij}^m = \varepsilon_{ij}^c$ from Eqs. (23), (28a) and (29a), by applying $\tilde{\varepsilon}_{22}^m(t) = \tilde{\varepsilon}_{33}^m(t) = 0$, $E_2^m = E_4^m = E_5^m = 1$, $E_1^m = E_3^m = 0$. Finally, one can obtain $Y_{ij}^{kl,m} = -\psi_m I_{ijkl}$ and

$$\sigma_{ij}^c = \sigma_{ij}^m = L_{ijkl}^{m,\infty} \varepsilon_{kl}^m + \psi_m L_{ijkl}^m * \dot{\varepsilon}_{kl}^m(t) = L_{ijkl}^{m,\infty} \varepsilon_{kl}^m + L_{ijkl}^{m,\text{iso}} * \dot{\varepsilon}_{kl}^m(t) \quad (38)$$

which traces back to the pure matrix case.

2.5 Influence of Component Parameters on Homogenization Relaxation Times

In this section, we analytically calculate the homogenization relaxation times $\tau_i, i = 1, 2, \dots, 5$ using known component parameters, investigating how fiber and matrix properties influence the overall viscoelastic response. It is important to note that relaxation time is closely related to material viscosity. A smaller viscosity results in a shorter relaxation time. When viscosity (η) approaches zero, the material behaves like an inviscid fluid, whereas when it approaches infinity, the material behaves like an elastic solid. We observe that changes in component parameters lead to variations in the homogenization relaxation times, with certain parameters exerting more significant influence compared to others.

We first investigate the influence of fiber parameters on homogenized relaxation times. Parameters are chosen as detailed in Table 1, with one parameter varied within specified ranges. Fig. 1a illustrates the impact of fiber volume fraction on viscoelastic behavior: as the fiber fraction increases, the relaxation times also increase, indicating that, in our research, fibrous composites with higher fiber content tend to exhibit more solid-like characteristics in the homogenized state. It is noteworthy that relaxation time associated with the fiber direction is always equal to the matrix relaxation time, as indicated by Eq. (36), implying that the viscoelastic behavior in this direction is solely influenced by matrix components, while viscoelastic behavior in other directions is influenced by both fiber and matrix components. Fig. 1b demonstrates how homogenized relaxation time varies with changes in $\nu_t^f = 0.20, 0.25, 0.35, 0.40$, revealing that ν_t^f has a limited impact on viscosity behavior. A slight decrease in homogenized relaxation time is observed with increasing ν_t^f .

Table 1: Material parameters of the fibrous composite material

Fiber	E_a^f	13,800	(MPa)	Young's modulus in axial direction
	E_t^f	9500	(MPa)	Young's modulus in transverse direction
	ν_{at}^f	0.28	[-]	Poisson's ratio in axial-transverse plane
	ν_t^f	0.4	[-]	Poisson's ratio in transverse plane
	μ_{at}^f	5200	(MPa)	Shear modulus in axial-transverse plane
Matrix	E_∞^m	4500	(MPa)	Young's modulus
	ν^m	0.35	[-]	Poisson's ratio
	E_{iso}^m	500–3500	(MPa)	Isotropic relaxation modulus
	τ_1^m	10	(s)	Relaxation time

Next, we explore the influence of matrix parameters on homogenized relaxation times. As shown in Fig. 2a, an increase in E_{iso}^m leads to higher homogenized relaxation times due to the corresponding increase in viscosity. Similarly, Fig. 2b demonstrates that higher E_∞^m results in increased

homogenization relaxation times, paralleling the trend observed in Fig. 1a. Fig. 2c indicates that ν^m has minimal impact on viscosity behavior, albeit showing a slight increase with higher ν^m .

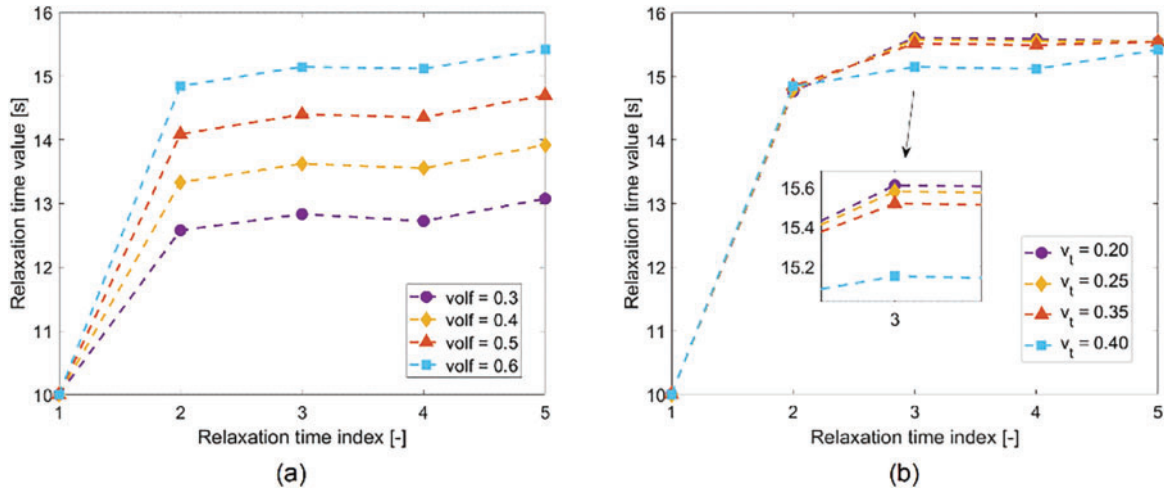


Figure 1: Influence of fiber parameters on homogenized relaxation times: (a) Fiber volume; (b) Poisson ratio in the transverse plane ν_t^f

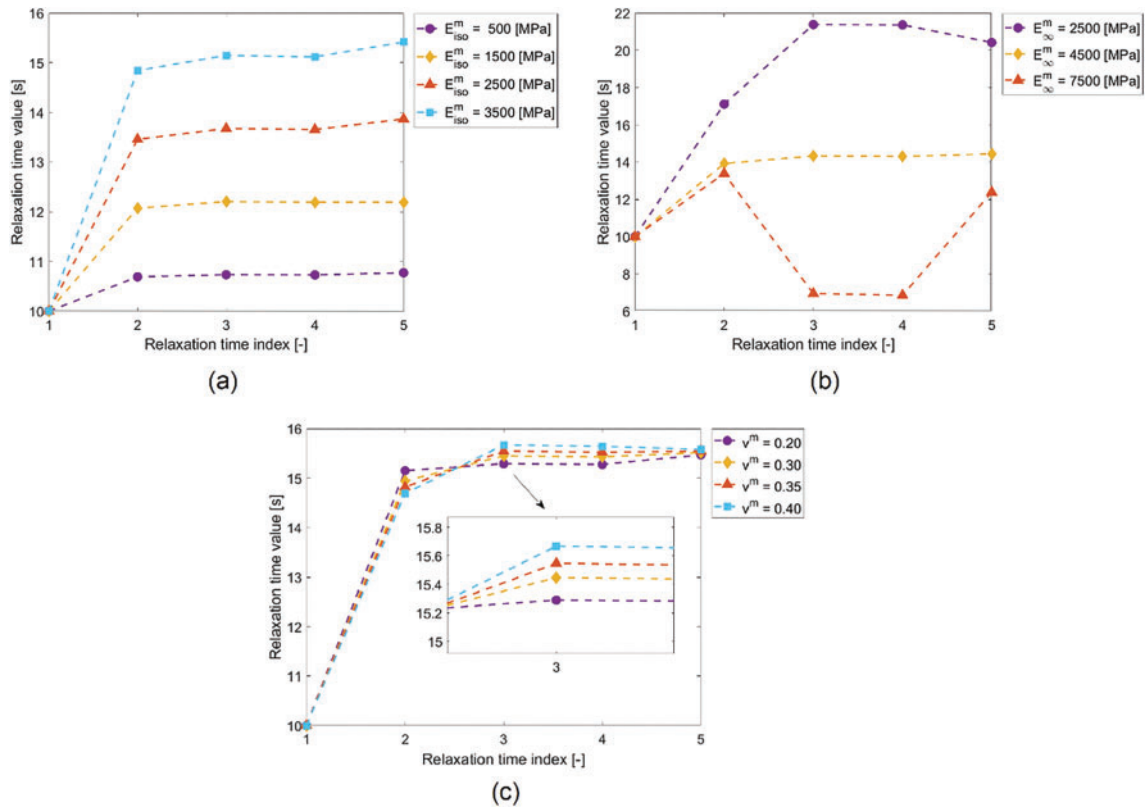


Figure 2: Influence of matrix parameters on homogenized relaxation times: (a) Relaxation modulus E_{iso}^m ; (b) Elastic modulus E_{∞}^m ; (c) Poisson ratio ν^m

2.6 Numerical Algorithm

In this section, we briefly introduce the numerical algorithm for the homogenized viscoelastic model of fibrous composite material. In finite element analysis, we update material stress as well as consistent tangent modulus over one increment $[t_n, t_{n+1}]$. The stress at t_{n+1} , namely, $\sigma_{ij}^{c,n+1}$ is given as

$$\begin{aligned}\sigma_{ij}^{c,n+1} &= L_{ijkl}^c \varepsilon_{kl}^{c,n+1} + A_{ijkl}^m \mu_{kl}^{m,n+1} = L_{ijkl}^c \varepsilon_{kl}^{c,n+1} + A_{ijkl}^m Y_{kl}^{st,m}(t) * \dot{\varepsilon}_{st}^{c,n+1}(t) \\ &= L_{ijkl}^c \varepsilon_{kl}^{c,n+1} + R_{ijkl}^c(t) * \dot{\varepsilon}_{kl}^{c,n+1}(t)\end{aligned}\quad (39)$$

again $R_{ijkl}^c(t) \equiv A_{ijmn}^m Y_{nm}^{kl,m}(t)$ is the homogeneous relaxation tensor. The second term in the right-hand-side of Eq. (39) is given by the classic integration form:

$$\begin{aligned}A_{ijkl}^m Y_{kl}^{st,m}(t) * \dot{\varepsilon}_{st}^{c,n+1}(t) &= A_{ijkl}^m \int_0^{t_{n+1}} Y_{kl}^{st,m}(t_{n+1} - \eta) \dot{\varepsilon}_{st}^c(\eta) d\eta \\ &= A_{ijkl}^m \int_0^{t_n} Y_{kl}^{st,m}(t_{n+1} - \eta) \dot{\varepsilon}_{st}^c(\eta) d\eta + A_{ijkl}^m \int_{t_n}^{t_{n+1}} Y_{kl}^{st,m}(t_{n+1} - \eta) \dot{\varepsilon}_{st}^c(\eta) d\eta\end{aligned}\quad (40)$$

The numerical integration scheme is the same as the classic viscoelastic stress update procedure. For example:

$$\begin{aligned}\int_0^{t_n} Y_{11}^{11,m}(t_{n+1} - \eta) \dot{\varepsilon}_{11}^{c,n+1}(\eta) d\eta &= \int_0^{t_n} -\psi_m e^{-(t_{n+1}-\eta)/\tau_1} \dot{\varepsilon}_{11}^c(\eta) d\eta \\ &= \int_0^{t_n} -\psi_m e^{-(t_{n+1}-t_n)/\tau_1} e^{-(t_n-\eta)/\tau_1} \dot{\varepsilon}_{11}^c(\eta) d\eta = e^{-\Delta t/\tau_1} \int_0^{t_n} -\psi_m e^{-(t_n-\eta)/\tau_1} \dot{\varepsilon}_{11}^c(\eta) d\eta\end{aligned}\quad (41a)$$

$$\int_{t_n}^{t_{n+1}} Y_{11}^{11,m}(t_{n+1} - \eta) \dot{\varepsilon}_{11}^{c,n+1}(\eta) d\eta = \int_{t_n}^{t_{n+1}} -\psi_m e^{-(t_{n+1}-\eta)/\tau_1} \dot{\varepsilon}_{11}^c(\eta) d\eta \approx -\psi_m e^{-\Delta t/(2\tau_1)} \Delta \varepsilon_{11}^c \quad (41b)$$

With $\Delta t \equiv t_{n+1} - t_n$, and $\Delta \varepsilon_{11}^c$ the incremental strain at 11 component.

From the convolution form in Eq. (36), define the following 9 state variables:

$$\begin{aligned}s_1^{n+1} &= \int_0^{t_{n+1}} e^{-(t_{n+1}-\eta)/\tau_1} \dot{\varepsilon}_{11}^c(\eta) d\eta, s_2^{n+1} = \int_0^{t_{n+1}} e^{-(t_{n+1}-\eta)/\tau_2} \dot{\varepsilon}_{11}^c(\eta) d\eta \\ s_3^{n+1} &= \int_0^{t_{n+1}} e^{-(t_{n+1}-\eta)/\tau_2} \dot{\varepsilon}_{22}^c(\eta) d\eta, s_4^{n+1} = \int_0^{t_{n+1}} e^{-(t_{n+1}-\eta)/\tau_3} \dot{\varepsilon}_{22}^c(\eta) d\eta \\ s_5^{n+1} &= \int_0^{t_{n+1}} e^{-(t_{n+1}-\eta)/\tau_2} \dot{\varepsilon}_{33}^c(\eta) d\eta, s_6^{n+1} = \int_0^{t_{n+1}} e^{-(t_{n+1}-\eta)/\tau_3} \dot{\varepsilon}_{33}^c(\eta) d\eta \\ s_7^{n+1} &= \int_0^{t_{n+1}} e^{-(t_{n+1}-\eta)/\tau_4} \dot{\varepsilon}_{23}^c(\eta) d\eta, s_8^{n+1} = \int_0^{t_{n+1}} e^{-(t_{n+1}-\eta)/\tau_5} \dot{\varepsilon}_{13}^c(\eta) d\eta \\ s_9^{n+1} &= \int_0^{t_{n+1}} e^{-(t_{n+1}-\eta)/\tau_5} \dot{\varepsilon}_{12}^c(\eta) d\eta,\end{aligned}\quad (42)$$

From (41a) and (41b), we can obtain

$$s_1^{n+1} = e^{-\Delta t/\tau_1} s_1^n + e^{-\Delta t/(2\tau_1)} \Delta \varepsilon_{11} \quad (43)$$

and

$$\left\{ \frac{\partial s_1^{n+1}}{\partial \varepsilon_{ij}^{c,n+1}} \right\} = [e^{-\Delta t/(2\tau_1)} \quad 0 \quad 0 \quad 0 \quad 0 \quad 0]^T \quad (44)$$

Similar equations can be derived for s_i^{n+1} , $i = 2, 3, \dots, 9$. Thus, Eq. (36) can be written with the aforementioned state variables that

$$\begin{aligned}
\mu_{11}^{m,n+1} &= -\psi_m s_1^{n+1} \\
\mu_{22}^{m,n+1} &= \frac{P_1^{mm} \psi_m}{P_2^{mm} + P_3^{mm}} s_1^{n+1} + \left[-\frac{\tau_2 - \tau_1}{\tau_2} \frac{E_1^m}{P_2^{mm} + P_3^{mm}} - \frac{\tau_1}{\tau_2} \frac{P_1^{mm} \psi_m}{P_2^{mm} + P_3^{mm}} \right] s_2^{n+1} \\
&\quad - \frac{\tau_2 - \tau_1}{\tau_2} \frac{E_2^m + E_3^m}{2(P_2^{mm} + P_3^{mm})} (s_3^{n+1} + s_5^{n+1}) - \frac{\tau_3 - \tau_1}{\tau_3} \frac{E_2^m - E_3^m}{2(P_2^{mm} - P_3^{mm})} (s_4^{n+1} - s_6^{n+1}) \\
\mu_{33}^{m,n+1} &= \frac{P_1^{mm} \psi_m}{P_2^{mm} + P_3^{mm}} s_1^{n+1} + \left[-\frac{\tau_2 - \tau_1}{\tau_2} \frac{E_1^m}{P_2^{mm} + P_3^{mm}} - \frac{\tau_1}{\tau_2} \frac{P_1^{mm} \psi_m}{P_2^{mm} + P_3^{mm}} \right] s_2^{n+1} \\
&\quad - \frac{\tau_2 - \tau_1}{\tau_2} \frac{E_2^m + E_3^m}{2(P_2^{mm} + P_3^{mm})} (s_3^{n+1} + s_5^{n+1}) + \frac{\tau_3 - \tau_1}{\tau_3} \frac{E_2^m - E_3^m}{2(P_2^{mm} - P_3^{mm})} (s_4^{n+1} - s_6^{n+1}) \\
\mu_{23}^{m,n+1} &= -\frac{\tau_4 - \tau_1}{\tau_4} \frac{E_4^m}{P_4^{mm}} s_7^{n+1} \\
\mu_{13}^{m,n+1} &= -\frac{\tau_5 - \tau_1}{\tau_5} \frac{E_5^m}{P_5^{mm}} s_8^{n+1} \\
\mu_{12}^{m,n+1} &= -\frac{\tau_5 - \tau_1}{\tau_5} \frac{E_5^m}{P_5^{mm}} s_9^{n+1}
\end{aligned} \tag{45}$$

In addition, one can derive $T_{ijkl}^m \equiv \partial \mu_{ij}^{m,n+1} / \partial \varepsilon_{kl}^{m,n+1}$ so that the consistent tangent material modulus is given as

$$\frac{\partial \sigma_{ij}^{c,n+1}}{\partial \varepsilon_{kl}^{c,n+1}} = L_{ijkl}^c + A_{ijmn}^m \frac{\partial \mu_{mn}^{m,n+1}}{\partial \varepsilon_{kl}^{c,n+1}} = L_{ijkl}^c + A_{ijmn}^m T_{mnkl}^m \tag{46}$$

Specifically,

$$\begin{aligned}
T_{1111}^m &= -\psi_m e^{-\Delta t / (2\tau_1)} \\
T_{2211}^m &= T_{3311}^m = \frac{P_1^{mm} \psi_m}{P_2^{mm} + P_3^{mm}} e^{-\Delta t / (2\tau_1)} + \left[-\frac{\tau_2 - \tau_1}{\tau_2} \frac{E_1^m}{P_2^{mm} + P_3^{mm}} - \frac{\tau_1}{\tau_2} \frac{P_1^{mm} \psi_m}{P_2^{mm} + P_3^{mm}} \right] e^{-\Delta t / (2\tau_2)} \\
T_{2222}^m &= T_{3333}^m = -\frac{\tau_2 - \tau_1}{\tau_2} \frac{E_2^m + E_3^m}{2(P_2^{mm} + P_3^{mm})} e^{-\Delta t / (2\tau_2)} - \frac{\tau_3 - \tau_1}{\tau_3} \frac{E_2^m - E_3^m}{2(P_2^{mm} - P_3^{mm})} e^{-\Delta t / (2\tau_3)} \\
T_{2233}^m &= T_{3322}^m = -\frac{\tau_2 - \tau_1}{\tau_2} \frac{E_2^m + E_3^m}{2(P_2^{mm} + P_3^{mm})} e^{-\Delta t / (2\tau_2)} + \frac{\tau_3 - \tau_1}{\tau_3} \frac{E_2^m - E_3^m}{2(P_2^{mm} - P_3^{mm})} e^{-\Delta t / (2\tau_3)} \\
T_{2323}^m &= -\frac{\tau_4 - \tau_1}{\tau_4} \frac{E_4^m}{P_4^{mm}} e^{-\Delta t / (2\tau_4)} \\
T_{1313}^m &= T_{1212}^m = -\frac{\tau_5 - \tau_1}{\tau_5} \frac{E_5^m}{P_5^{mm}} e^{-\Delta t / (2\tau_5)}
\end{aligned} \tag{47}$$

3 Numerical Examples and Validation

In this section, we propose several groups of numerical examples to verify and validate the proposed analytical homogenized viscoelastic model for fibrous composite materials. The numerical examples and validation are organized as follows: In [Section 3.1](#), unit cell tests under uniaxial tension and pure shear conditions are performed to demonstrate consistency between FEM and the proposed homogenized model under a uniform strain field. In [Sections 3.2](#) and [3.3](#), we introduce pure bending beam experiments and torsion experiments to further investigate the ability of the proposed homogenized method. In [Section 3.4](#), theoretical predictions are compared with experimental results from the literature to validate prediction accuracy. All simulations are conducted using the commercial FEM software ABAQUS/Standard 2022 with a user material subroutine (UMAT).

3.1 Unit Cell Tests

We first verify the accuracy of the homogenized viscoelastic model using a uniform strain field problem. We explicitly construct a unit cell of the fibrous composite material for the direct numerical simulation (DNS), where the fiber is transversely isotropic elastic and the matrix follows the standard solid model, as depicted in [Fig. 3](#). The size of the unit cell is set as $l_x = 1.732$ (mm), $l_y = 1$ (mm), and $l_z = 0.5$ (mm). By applying periodic boundary conditions and a macroscopic strain history, we obtain the corresponding averaged stress history. For comparison, we construct a one-element model associated with the homogenized viscoelastic constitutive model and apply the same strain history. [Table 1](#) lists the parameters for both the fiber and the matrix phases.

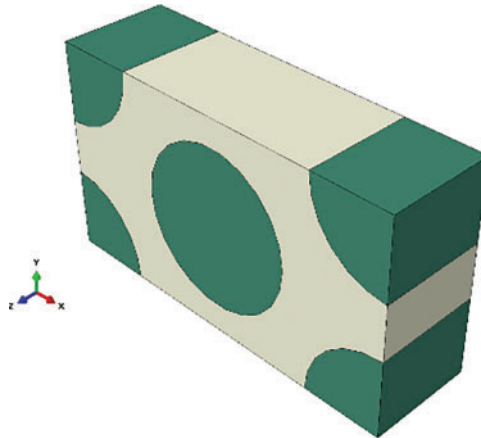


Figure 3: Unit cell model with size of $l_x = 1.732$ (mm), $l_y = 1$ (mm), $l_z = 0.5$ (mm)

Various numerical tests are proposed with different fiber volume fractions: $c^f = 0.3, 0.4, 0.5, 0.6$ and different relaxation moduli: $E_{iso}^m = 500, 1500, 2500, 3500$ (MPa). For each unit cell problem, we perform three uniaxial tension tests in the x -, y -, and z -direction, and three pure shear tests in the xy -, xz -, and yz - planes, where x refers to the axial direction of the fiber. In order to capture the viscoelastic response, we apply a loading-holding-unloading curve for the prescribed macroscopic strain, as depicted in [Fig. 4](#). In the unit cell problem, we use the loading rate defined in [Fig. 4a](#). For pure bending and torsion tests, the loading rate is defined as in [Fig. 4b](#) for a clearer observation of the viscoelastic response.

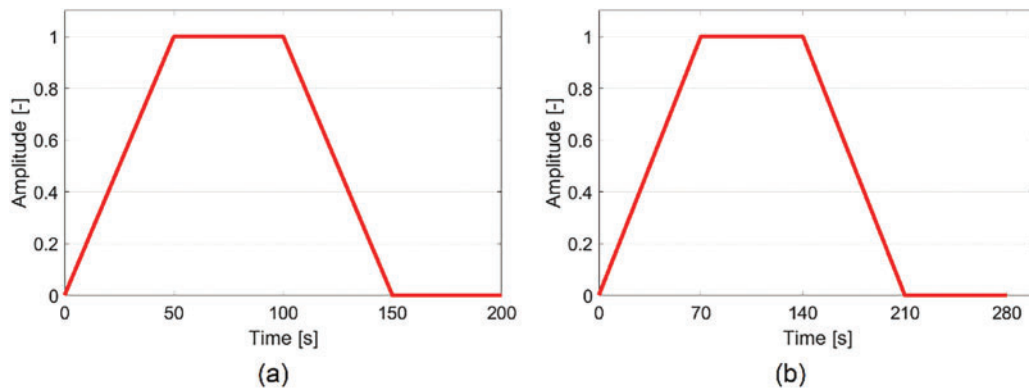


Figure 4: Loading rates: (a) Unit cell test; (b) Pure bending and torsion tests

A group of DNS simulations is depicted in Fig. 5, while the corresponding group of one-element simulation using the proposed homogenized viscoelastic constitutive model is depicted in Fig. 6. Clearly, the DNS results provide more detail but at a higher computational cost. To avoid redundancy, not all simulation results will be displayed. Figs. 7 and 8 show comparison of strain-stress responses between the DNS and the homogenized model (HM for short) for $E_{iso}^m = 500$ (MPa) and $E_{iso}^m = 3500$ (MPa). Note that the x -direction of the material coordinate system coincides with the z -direction of the overall coordinate system. Figs. 7c and 8c show that the composite response is fiber-dominated in this direction, while in other directions, the response is matrix-dominated. A more significant viscoelastic response is observed as E_{iso}^m increases. All the results show good agreement between the homogenized model and the DNS simulations.

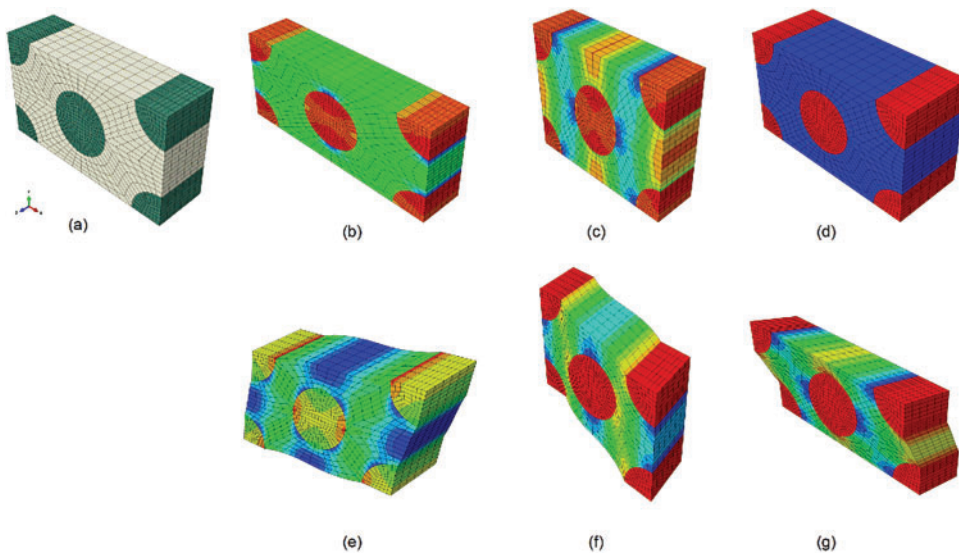


Figure 5: Demonstrations of DNS model and six loading cases: (a) Honeycomb unit cell; (b) uniaxial tension test in x -direction; (c) uniaxial tension test in y -direction; (d) uniaxial tension test in z -direction; (e) pure shear test in xy plane; (f) pure shear test in xz plane; (g) pure shear test in yz plane

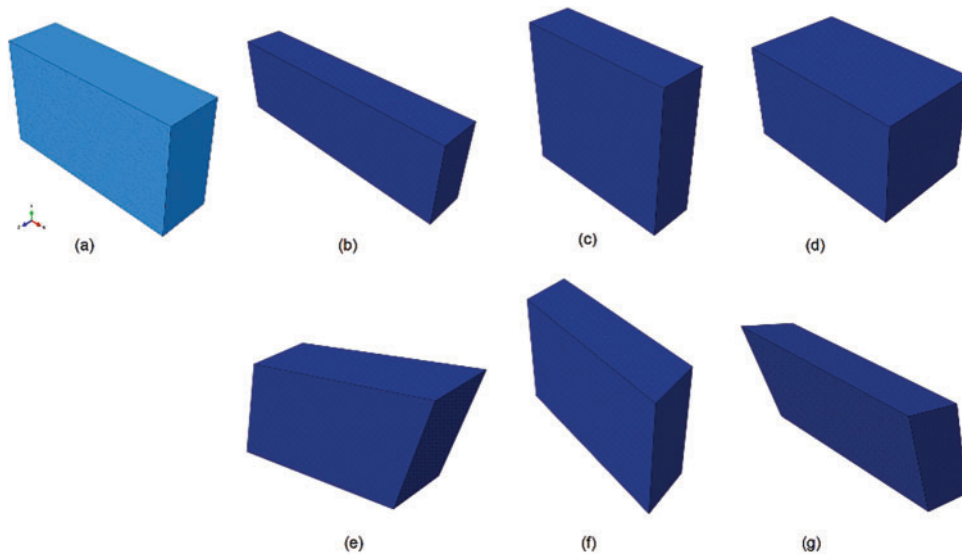


Figure 6: Demonstrations of homogenized model and six loading cases: (a) One-element model; (b) uniaxial tension test in x -direction; (c) uniaxial tension test in y -direction; (d) uniaxial tension test in z -direction; (e) pure shear test in xy plane; (f) pure shear test in xz plane; (g) pure shear test in yz plane

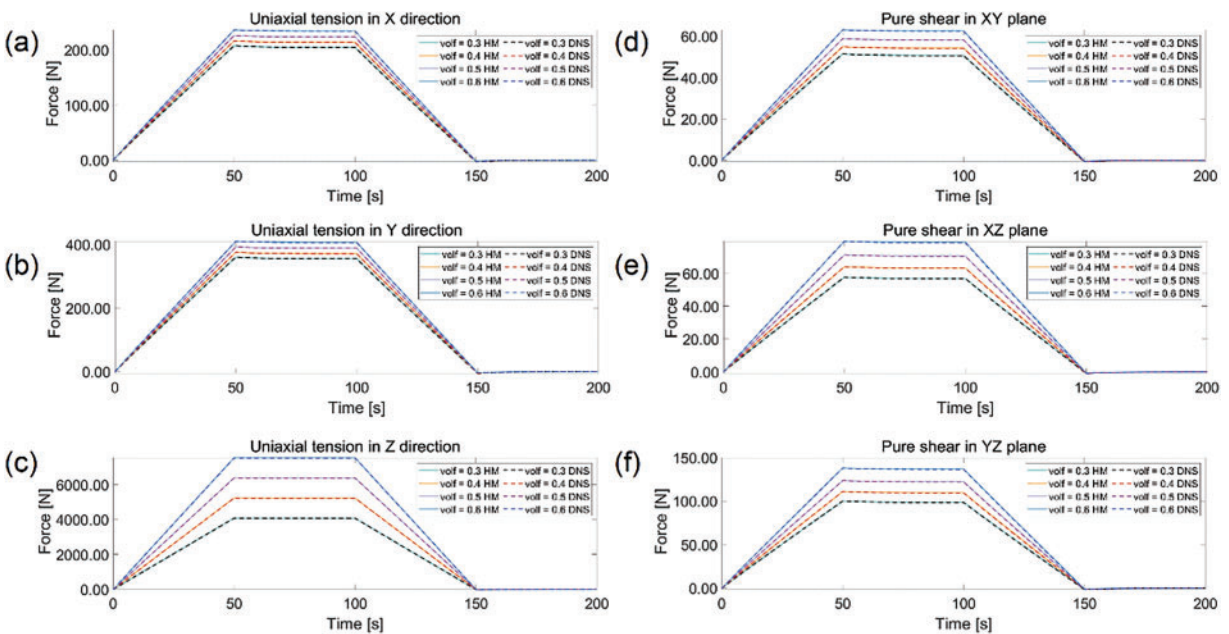


Figure 7: Relaxation curves under different fiber volume ratios with $E_{iso}^m = 500$ (MPa): uniaxial tension test in (a) x -direction; (b) y -direction; (c) z -direction; pure shear test in (d) xy plane; (e) xz plane; (f) yz plane

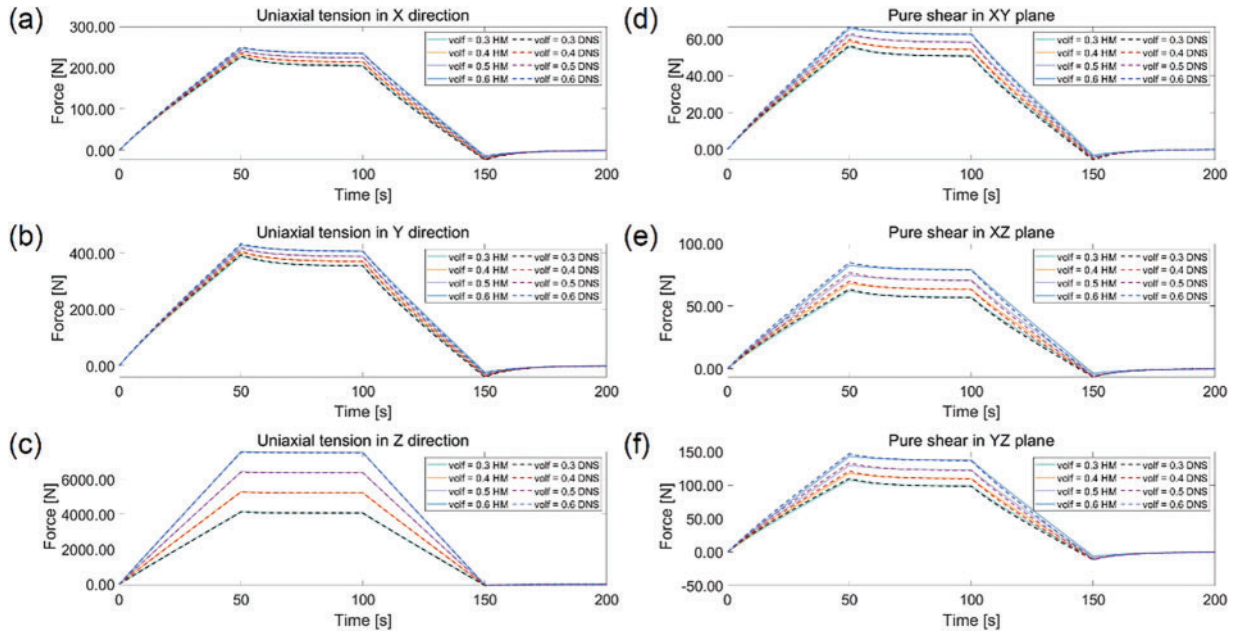


Figure 8: Relaxation curves under different fiber volume ratios with $E_{iso}^m = 3500$ (MPa): uniaxial tension test in (a) x -direction; (b) y -direction; (c) z -direction; pure shear test in (d) xy plane; (e) xz plane; (f) yz plane

3.2 Pure Bending Tests

The unit cell tests verify the homogenized viscoelastic model under uniform strain fields. To extend this validation to non-uniform strain fields, we propose a series of pure bending tests with geometric setups and boundary conditions outlined in Fig. 9. The size of beam is $l_x = 39.836$ (mm), $l_y = 5$ (mm), $l_z = 7$ (mm). The applied moment $M(t)$ follows the loading rate defined in Fig. 4b, with a maximum value of $M_{max} = 50$ (N · mm). Both direct numerical simulation (DNS) and homogenized models, as illustrated in Fig. 10, are employed to compare numerical efficiency and accuracy. The results are presented in Fig. 11. It is observed that the stress concentration effect cannot be effectively captured due to the piecewise constant eigenstrain assumption. This approach sacrifices some detail for the sake of efficiency.

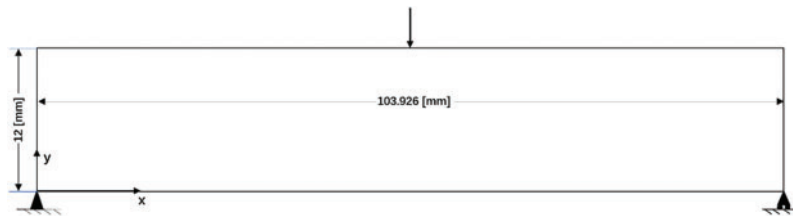


Figure 9: Geometric setup of pure bending beam and boundary conditions

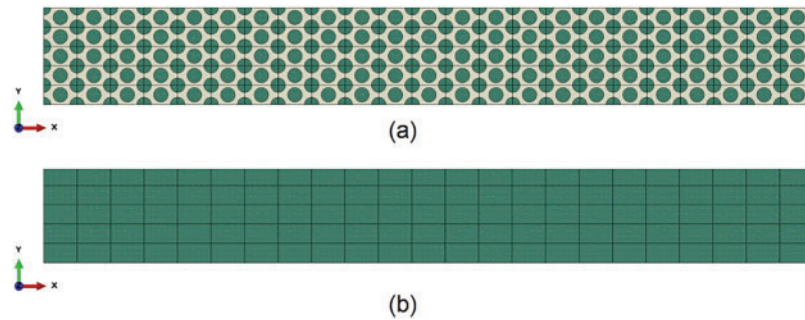


Figure 10: Pure bending beam models: (a) DNS; (b) homogenized model

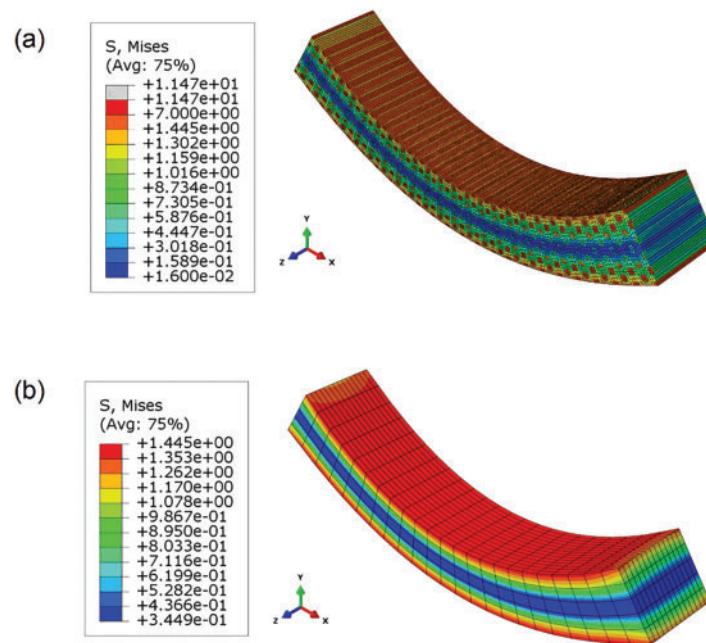


Figure 11: Pure bending beam simulation result demonstrations: (a) DNS; (b) homogenized model

We tested different fiber volume fractions, $c^f = 0.3, 0.4, 0.5, 0.6$, with the matrix relaxation moduli set to $E_{\text{iso}}^m = 3000$ (MPa). The results of the homogenized model and the reference results for comparison are shown in Fig. 12. We used the displacement at $t = 100$ (s) to estimate the relative displacement error between the DNS and homogenized models, as depicted in Fig. 13. The proposed method demonstrates good consistency with the DNS method, with relative errors below 3%. It is also noteworthy that the DNS method takes approximately 7600 (s), while the homogenized model requires only 50 (s). The simulation is significantly faster than DNS, and the overall response remains highly accurate.

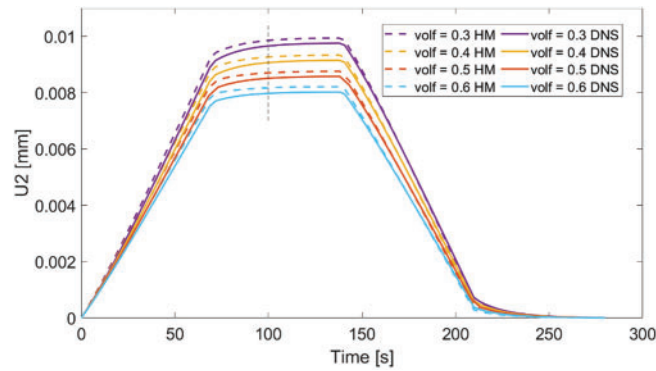


Figure 12: Pure bending beam experiment under different fiber volume fractions: DNS and homogenized model result comparison with $E_{\text{iso}}^m = 3000$ (MPa)

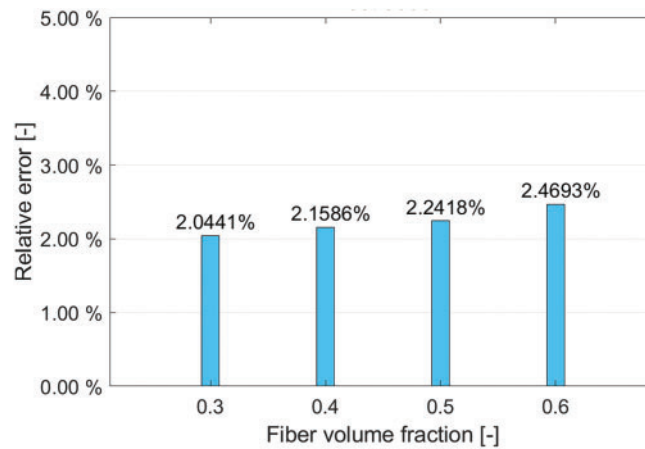


Figure 13: Pure bending beam tests under different fiber volume fractions: displacement relative error between DNS and homogenized model result with $E_{\text{iso}}^m = 3000$ (MPa)

3.3 Torsion Tests

In this section, the beam used for the pure bending tests is employed to conduct torsion tests. We select viscoelastic parameters as $E_{\text{iso}}^m = 3000$ (MPa) and investigate creep behavior under four sets of fiber volume fractions: $c^f = 0.3, 0.4, 0.5, 0.6$. The left boundary of the beam is fixed, and a moment of $M_{\text{max}} = 500$ (N · mm) is applied to the right boundary with the loading rate shown in Fig. 4b. The simulation results for both the DNS and homogenized models are demonstrated in Fig. 14. The comparison of relaxation curves is depicted in Fig. 15. It is evident from the analysis that the discrepancy between the two curves is minimal, suggesting that the proposed model effectively captures torsional deformation.

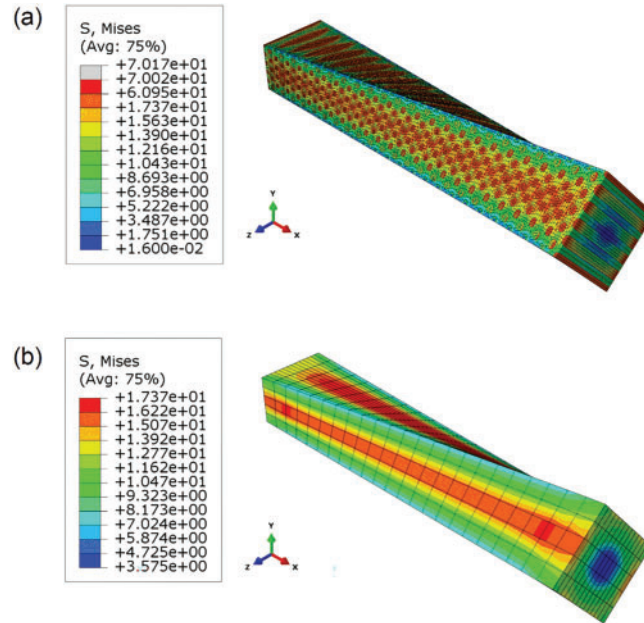


Figure 14: Beam torsion simulation result demonstrations: (a) DNS; (b) homogenized model

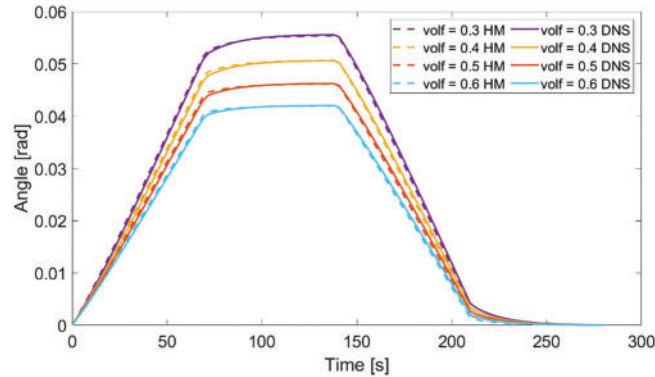


Figure 15: Beam torsion experiment under different fiber volume fractions, DNS and homogenized model result comparison with $E_{\text{iso}}^m = 3000$ (MPa)

3.4 Experiment Validation

We obtained experimental data from a paper published by Thiruppukuzhi et al. [52] and referenced another paper by Chen et al. [53]. In the first paper, Thiruppukuzhi et al. conducted experiments using S2-glass/8553-40 epoxy fiber-reinforced composite with a fiber volume fraction of 65%. They performed a series of off-axial tensile tests at three strain rates: 0.0001 [1/s], 0.01 [1/s], 1 [1/s], and four off-axial tensile directions: 0°, 15°, 30°, and 90°. The combination of loading strain rate and off-axis tensile direction in the experiment is shown in Table 2, where markers represent the experiments conducted under the corresponding combinations. The setup of off-axial tensile tests is illustrated in Fig. 16. The specimen dimensions are $l_x = 100$ (mm), $l_y = 17.8$ (mm) as described in the original experiment, and we set $l_z = 1$ (mm). We simulate the actual experimental boundary conditions by

clamping the two ends of the specimen with fixtures, resulting in an over-constrained setup. Symmetric boundary conditions are applied in the z -direction to represent the specimen's real-life thickness.

Table 2: Combination of loading strain rate and off-axis tensile direction in the experiment

		0°	15°	30°	90°
0.0001	[1/s]	<input type="checkbox"/>	<input type="checkbox"/>	<input type="checkbox"/>	<input type="checkbox"/>
0.01	[1/s]		<input type="checkbox"/>	<input type="checkbox"/>	
1	[1/s]		<input type="checkbox"/>	<input type="checkbox"/>	

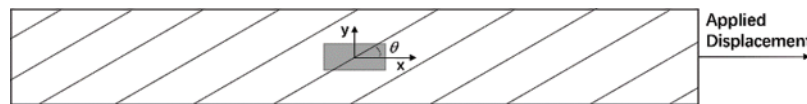


Figure 16: Setup of off-axis tensile tests

The elastic material parameters of both the fiber and matrix are identified inversely using experimental data of composite materials under two sets of conditions: 0.0001 [1/s], 0° and 0.0001 [1/s], 90°. The viscoelastic material parameters for the matrix are determined using experimental data with the following test conditions: 0.0001 [1/s], 15°, 0.01 [1/s], 15°, and 1 [1/s], 15°. Table 3 presents the material parameters of the fiber and matrix obtained by fitting the experimental data. Fig. 17 shows the homogenized model results and experimental data along the 0°, 15°, 30°, 90° directions under a loading strain rate of 0.0001 [1/s]. The simulation results along the 15° and 30° directions also show good agreement with the experimental data, indicating that the parameters are a good fit. The Von Mises stress contour plots for the homogenized models along the four directions are shown in Fig. 18. Theoretical predictions begin to diverge from experimental results due to significant nonlinearity induced by plasticity or damage at relatively large strains.

Table 3: Material parameters for fibrous composite material in experiment

Fiber	E^m	71,000	(MPa)	Young's modulus
	ν^f	0.2	[–]	Poisson's ratio
Matrix	E_∞^m	1900	(MPa)	Young's modulus
	ν^m	0.35	[–]	Poisson's ratio
	E_∞^{iso}	304	(MPa)	Isotropic relaxation modulus
	τ_1^m	0.8	(s)	Relaxation time

Figs. 19 and 20 present the homogenized model results and experimental data along directions 15°, 30° under loading strain rates of 0.01 [1/s] and 1 [1/s], respectively. The corresponding Von Mises stress contour plots for the homogenized models are shown in Figs. 21 and 22. The experimental data along 15° were used to fit the viscoelastic parameters, while the data along 30° were used to validate the accuracy of the proposed homogenized model. From Figs. 19 and 20, the simulation results along 30° exhibit good consistency with experimental data, indicating that our homogenized model can provide reasonable predictions for fibrous composite materials with viscoelastic effects.

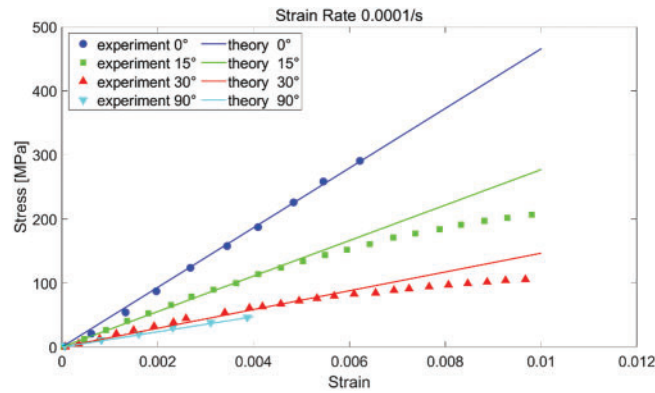


Figure 17: Strain-stress curves obtained from experiment results and homogenized model predictions for four off-axis tensile directions 0° , 15° , 30° , and 90° , loading strain rate $\dot{\epsilon} = 0.0001$ [1/s]

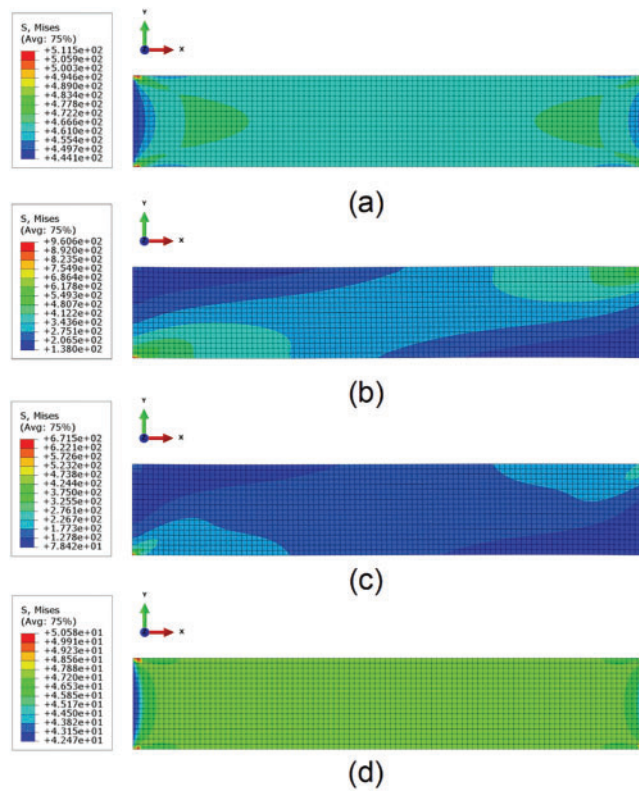


Figure 18: Von Mises stress cloud for homogenized models of four off-axis tensile directions: (a) 0° ; (b) 15° ; (c) 30° ; (d) 90° , loading strain rate $\dot{\epsilon} = 0.0001$ [1/s]

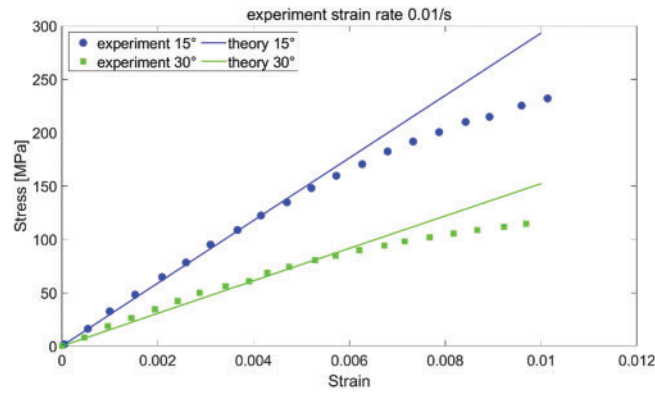


Figure 19: Strain-stress curves obtained from experiment results and homogenized model predictions for two off-axis tensile directions 15°, 30°, loading strain rate $\dot{\epsilon} = 0.01$ [1/s]

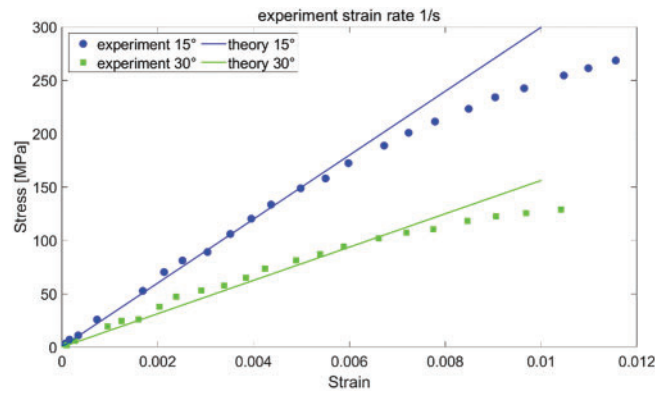


Figure 20: Strain-stress curves obtained from experiment results and homogenized model predictions for two off-axis tensile directions 15°, 30°, loading strain rate $\dot{\epsilon} = 1$ [1/s]

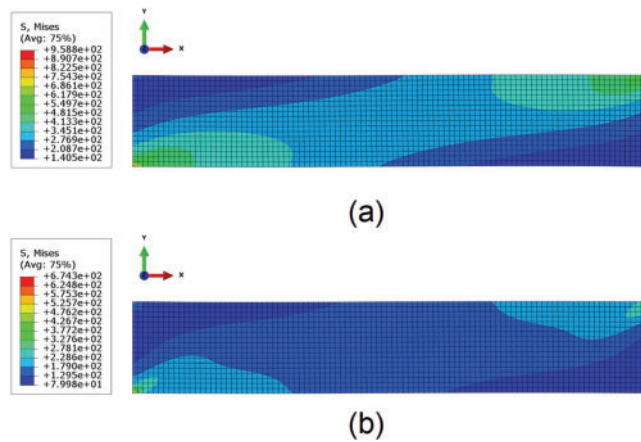


Figure 21: Von Mises stress contour plot for homogenized models of two off-axis tensile directions: (a) 15°; (b) 30°, loading strain rate $\dot{\epsilon} = 0.01$ [1/s]

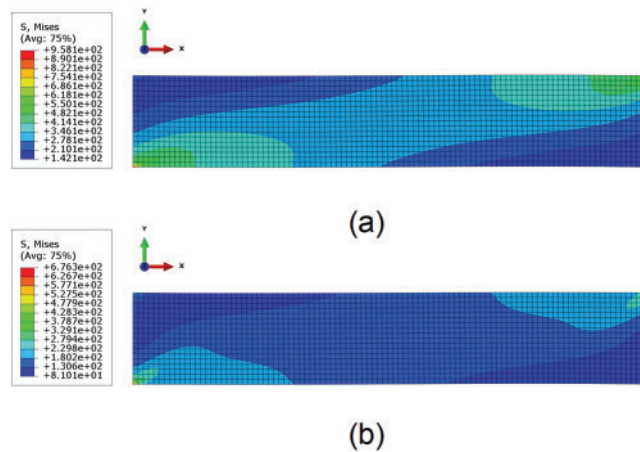


Figure 22: Von Mises stress contour plot for homogenized models of two off-axis tensile directions: (a) 15°; (b) 30°, loading strain rate $\dot{\epsilon} = 1$ [1/s]

4 Conclusion

In this manuscript, we propose an analytical homogenized viscoelastic model for fibrous composite materials using the reduced-order homogenization (ROH) method. Compared to numerical homogenization methods, our analytical model significantly reduces simulation costs while providing accurate predictions of the overall mechanical behavior. However, some deviations in local stress are observed, attributable to the one-partition-per-phase assumption. We model the fiber phase as transversely isotropic elastic, while the matrix phase follows a standard solid model. This approach allows for the analytical determination of effective moduli and relaxation times in fibrous composites. As the fiber volume fraction approaches zero, our homogenized viscoelastic model simplifies to a pure viscoelastic model. We verify our model through numerical unit cell tests, pure bending beam tests, and torsion tests, demonstrating its accuracy and computational efficiency compared to direct numerical simulations. Experimental validations further confirm the reliability of our approach.

Acknowledgement: The authors would like to acknowledge the support of the National Key R&D Program of China and the National Natural Science Foundation of China. The research is also supported by Peking University for this publication.

Funding Statement: Financial support by the National Key R&D Program of China (Grant No. 2023YFA1008901) and the National Natural Science Foundation of China (Grant Nos. 11988102, 12172009) is gratefully acknowledged. The research is also supported by “The Fundamental Research Funds for the Central Universities, Peking University”.

Author Contributions: The authors confirm contribution to the paper as follows: Huilin Jia contributed to the formula derivation, and simulation. Shanqiao Huang assisted in offering methodology and revising the manuscript. Zifeng Yuan contributed to the initial idea, the overall structure and final editing of the manuscript. All authors reviewed the results and approved the final version of the manuscript.

Availability of Data and Materials: Data available on request from the authors.

Ethics Approval: Not applicable.

Conflicts of Interest: The authors declare no conflicts of interest to report regarding the present study.

References

- [1] Z. Guo *et al.*, “3D printing of curvilinear fiber reinforced variable stiffness composite structures: A review,” *Compos. Part B Eng.*, vol. 272, no. 1, 2024, Art. no. 112039. doi: [10.1016/j.compositesb.2024.112039](https://doi.org/10.1016/j.compositesb.2024.112039).
- [2] P. Aduwenye, B. W. Chong, P. Gujar, and X. Shi, “Mechanical properties and durability of carbon fiber reinforced cementitious composites: A review,” *Constr. Build. Mater.*, vol. 452, 2024, Art. no. 138822. doi: [10.1016/j.conbuildmat.2024.138822](https://doi.org/10.1016/j.conbuildmat.2024.138822).
- [3] Z. Li, B. Wang, P. Hao, K. Du, Z. Mao and T. Li, “Multi-scale numerical calculations for the interphase mechanical properties of carbon fiber reinforced thermoplastic composites,” *Compos. Sci. Technol.*, vol. 260, 2025, Art. no. 110982. doi: [10.1016/j.compscitech.2024.110982](https://doi.org/10.1016/j.compscitech.2024.110982).
- [4] M. Mohammed *et al.*, “A review on the advancement of renewable natural fiber hybrid composites: Prospects, challenges, and industrial applications,” *J. Renew. Mater.*, vol. 12, pp. 1237–1290, 2024. doi: [10.32604/jrm.2024.051201](https://doi.org/10.32604/jrm.2024.051201).
- [5] H. Awais, Y. Nawab, A. Amjad, A. Anjang, H. M. Akil and M. S. Z. Abidin, “Environmental benign natural fibre reinforced thermoplastic composites: A review,” *Compos. Part C Open Access*, vol. 4, 2021, Art. no. 100082. doi: [10.1016/j.jcomc.2020.100082](https://doi.org/10.1016/j.jcomc.2020.100082).
- [6] B. Nedjar, “A time dependent model for unidirectional fibre-reinforced composites with viscoelastic matrices,” *Int. J. Solids Struct.*, vol. 48, no. 16–17, pp. 2333–2339, 2011. doi: [10.1016/j.ijsolstr.2011.04.007](https://doi.org/10.1016/j.ijsolstr.2011.04.007).
- [7] U. Hofer, M. Luger, R. Traxl, and R. Lackner, “Closed-form expressions for effective viscoelastic properties of fiber-reinforced composites considering fractional matrix behavior,” *Mech. Mater.*, vol. 127, pp. 14–25, 2018. doi: [10.1016/j.mechmat.2018.08.005](https://doi.org/10.1016/j.mechmat.2018.08.005).
- [8] Q. Chen, G. Chatzigeorgiou, and F. Meraghni, “Extended mean-field homogenization of viscoelastic-viscoplastic polymer composites undergoing hybrid progressive degradation induced by interface debonding and matrix ductile damage,” *Int. J. Solids Struct.*, vol. 210–211, pp. 1–17, 2021. doi: [10.1016/j.ijsolstr.2020.11.017](https://doi.org/10.1016/j.ijsolstr.2020.11.017).
- [9] C. A. Suarez-Afanador, N. Lahellec, and M. I. Idiart, “Mean-field descriptions for the viscoelastic response of thermorheologically complex reinforced solids,” *Eur. J. Mech. A Solids*, vol. 98, 2023, Art. no. 104859. doi: [10.1016/j.euromechsol.2022.104859](https://doi.org/10.1016/j.euromechsol.2022.104859).
- [10] P. Lenz and R. Mahnken, “Multiscale simulation of polymer curing of composites combined mean-field homogenisation methods at large strains,” *Int. J. Solids Struct.*, vol. 290, no. 2, 2024, Art. no. 112642. doi: [10.1016/j.ijsolstr.2023.112642](https://doi.org/10.1016/j.ijsolstr.2023.112642).
- [11] Q. Li, W. Chen, S. Liu, and J. Wang, “A novel implementation of asymptotic homogenization for viscoelastic composites with periodic microstructures,” *Compos. Struct.*, vol. 208, no. 1–3, pp. 276–286, 2019. doi: [10.1016/j.compstruct.2018.09.056](https://doi.org/10.1016/j.compstruct.2018.09.056).
- [12] Y. -M. Yi, S. -H. Park, and S. -K. Youn, “Asymptotic homogenization of viscoelastic composites with periodic microstructures,” *Int. J. Solids Struct.*, vol. 35, no. 17, pp. 2039–2055, 1998. doi: [10.1016/S0020-7683\(97\)00166-2](https://doi.org/10.1016/S0020-7683(97)00166-2).
- [13] I. V. Andrianov, V. V. Danishevs’kyy, and D. Weichert, “Homogenization of viscoelastic-matrix fibrous composites with square-lattice reinforcement,” *Arch. Appl. Mech.*, vol. 81, no. 12, pp. 1903–1913, 2011. doi: [10.1007/s00419-011-0526-z](https://doi.org/10.1007/s00419-011-0526-z).
- [14] C. Badulescu, N. Lahellec, and P. Suquet, “Field statistics in linear viscoelastic composites and polycrystals,” *Eur. J. Mech. A Solids*, vol. 49, pp. 329–344, 2015. doi: [10.1016/j.euromechsol.2014.07.012](https://doi.org/10.1016/j.euromechsol.2014.07.012).
- [15] G. Debotton and L. Tevet-Deree, “The response of a fiber-reinforced composite with a viscoelastic matrix phase,” *J. Compos. Mater.*, vol. 38, no. 14, pp. 1255–1277, 2004. doi: [10.1177/0021998304042732](https://doi.org/10.1177/0021998304042732).
- [16] K. Kowalczyk-Gajewska and H. Petryk, “Sequential linearization method for viscous/elastic heterogeneous materials,” *Eur. J. Mech. A Solids*, vol. 30, no. 5, pp. 650–664, 2011. doi: [10.1016/j.euromechsol.2011.04.002](https://doi.org/10.1016/j.euromechsol.2011.04.002).

- [17] R. Brenner, R. Masson, O. Castelnau, and A. Zaoui, "A quasi-elastic affine formulation for the homogenised behaviour of nonlinear viscoelastic polycrystals and composites," *Eur. J. Mech. A Solids*, vol. 21, no. 6, pp. 943–960, 2002. doi: [10.1016/S0997-7538\(02\)01247-0](https://doi.org/10.1016/S0997-7538(02)01247-0).
- [18] H. Zhai, T. Bai, Q. Wu, N. Yoshikawa, K. Xiong and C. Chen, "Time-domain asymptotic homogenization for linear-viscoelastic composites: Mathematical formulae and finite element implementation," *Compos. Part C Open Access*, vol. 8, 2022, Art. no. 100248. doi: [10.1016/j.jcomc.2022.100248](https://doi.org/10.1016/j.jcomc.2022.100248).
- [19] Y. Liu, F. P. V. der Meer, L. J. Sluys, and J. T. Fan, "A numerical homogenization scheme used for derivation of a homogenized viscoelastic-viscoplastic model for the transverse response of fiber-reinforced polymer composites," *Compos. Struct.*, vol. 252, no. 1, 2020, Art. no. 112690. doi: [10.1016/j.compstruct.2020.112690](https://doi.org/10.1016/j.compstruct.2020.112690).
- [20] A. Carini, F. Genna, and F. Levi, "Time domain analytical bounds to the homogenized viscous kernels of linear viscoelastic composites," *Eur. J. Mech. A Solids*, vol. 102, no. 6, 2023, Art. no. 105108. doi: [10.1016/j.euromechsol.2023.105108](https://doi.org/10.1016/j.euromechsol.2023.105108).
- [21] C. Mareau, V. Favier, B. Weber, A. Galtier, and M. Berveiller, "Micromechanical modeling of the interactions between the microstructure and the dissipative deformation mechanisms in steels under cyclic loading," *Int. J. Plast.*, vol. 32–33, pp. 106–120, 2012. doi: [10.1016/j.ijplas.2011.12.004](https://doi.org/10.1016/j.ijplas.2011.12.004).
- [22] M. Zecevic and M. Knezevic, "Latent hardening within the elasto-plastic self-consistent polycrystal homogenization to enable the prediction of anisotropy of AA6022-T4 sheets," *Int. J. Plast.*, vol. 105, pp. 141–163, 2018. doi: [10.1016/j.ijplas.2018.02.007](https://doi.org/10.1016/j.ijplas.2018.02.007).
- [23] Y. Rémond, "Constitutive modelling of viscoelastic unloading of short glass fibre-reinforced polyethylene," *Compos. Sci. Technol.*, vol. 65, no. 3–4, pp. 421–428, 2005. doi: [10.1016/j.compscitech.2004.09.010](https://doi.org/10.1016/j.compscitech.2004.09.010).
- [24] O. Pierard and I. Doghri, "Study of various estimates of the macroscopic tangent operator in the incremental homogenization of elastoplastic composites," *Int. J. Multiscale Comput. Eng.*, vol. 4, no. 4, pp. 521–543, 2006. doi: [10.1615/IntJMCompEng.v4.i4.80](https://doi.org/10.1615/IntJMCompEng.v4.i4.80).
- [25] P. Suquet, "Overall properties of nonlinear composites: A modified secant moduli theory and its link with Ponte Castañeda's nonlinear variational procedure," *Comptes Rendus Académie Sci. Sér. II Mécanique Phys. Chim. Astron.*, vol. 320, pp. 563–571, 1995.
- [26] C. Bleiler, P. P. Castañeda, and O. Röhrle, "Tangent second-order homogenisation estimates for incompressible hyperelastic composites with fibrous microstructures and anisotropic phases," *J. Mech. Phys. Solids*, vol. 147, no. 4, 2021, Art. no. 104251. doi: [10.1016/j.jmps.2020.104251](https://doi.org/10.1016/j.jmps.2020.104251).
- [27] M. Barral, G. Chatzigeorgiou, F. Meraghni, and R. Léon, "Homogenization using modified Mori-Tanaka and TFA framework for elastoplastic-viscoelastic-viscoplastic composites: Theory and numerical validation," *Int. J. Plast.*, vol. 127, no. 2–3, p. 102632, 2020. doi: [10.1016/j.ijplas.2019.11.011](https://doi.org/10.1016/j.ijplas.2019.11.011).
- [28] G. J. Dvorak and Y. Benveniste, "On transformation strains and uniform fields in multiphase elastic media," *Proc. R Soc. Lond A*, vol. 437, no. 1900, pp. 291–310, 1992. doi: [10.1098/rspa.1992.0062](https://doi.org/10.1098/rspa.1992.0062).
- [29] J. C. Michel and P. Suquet, "Nonuniform transformation field analysis," *Int. J. Solids Struct.*, vol. 40, no. 25, pp. 6937–6955, 2003. doi: [10.1016/S0020-7683\(03\)00346-9](https://doi.org/10.1016/S0020-7683(03)00346-9).
- [30] J. C. Michel and P. Suquet, "Computational analysis of nonlinear composite structures using the nonuniform transformation field analysis," *Comput. Methods Appl. Mech. Eng.*, vol. 193, no. 48–51, pp. 5477–5502, 2004. doi: [10.1016/j.cma.2003.12.071](https://doi.org/10.1016/j.cma.2003.12.071).
- [31] J. Fish, V. Filonova, and Z. Yuan, "Hybrid impotent-incompatible eigenstrain based homogenization," *Int. J. Numer. Methods Eng.*, vol. 95, no. 1, pp. 1–32, 2013. doi: [10.1002/nme.4473](https://doi.org/10.1002/nme.4473).
- [32] E. Sanchez-Palencia, *Non-Homogeneous Media and Vibration Theory*. Berlin, Heidelberg: Springer, 1980, vol. 127. doi: [10.1007/3-540-10000-8](https://doi.org/10.1007/3-540-10000-8).
- [33] G. Papanicolau, A. Bensoussan, and J. L. Lions, *Asymptotic Analysis for Periodic Structures*. New York, USA: Elsevier North-Holland, 1978.
- [34] Q. Yu and J. Fish, "Multiscale asymptotic homogenization for multiphysics problems with multiple spatial and temporal scales: A coupled thermo-viscoelastic example problem," *Int. J. Solids Struct.*, vol. 39, no. 26, pp. 6429–6452, 2002. doi: [10.1016/S0020-7683\(02\)00255-X](https://doi.org/10.1016/S0020-7683(02)00255-X).

- [35] Y. Rahali, M. Assidi, I. Goda, A. Zghal, and J. F. Ganghoffer, "Computation of the effective mechanical properties including nonclassical moduli of 2.5D and 3D interlocks by micromechanical approaches," *Compos. Part B Eng.*, vol. 98, no. 10, pp. 194–212, 2016. doi: [10.1016/j.compositesb.2016.04.066](https://doi.org/10.1016/j.compositesb.2016.04.066).
- [36] T. J. R. Hughes, J. A. Cottrell, and Y. Bazilevs, "Isogeometric analysis: CAD, finite elements, NURBS, exact geometry and mesh refinement," *Comput. Methods Appl. Mech. Eng.*, vol. 194, no. 39–41, pp. 4135–4195, 2005. doi: [10.1016/j.cma.2004.10.008](https://doi.org/10.1016/j.cma.2004.10.008).
- [37] J. A. Cottrell, T. J. Hughes, and Y. Bazilevs, *Isogeometric Analysis: Toward Integration of CAD and FEA*. The Atrium, Southern Gate, Chichester, West Sussex, UK: John Wiley & Sons, 2009.
- [38] S. Matsubara, S. -N. Nishi, and K. Terada, "On the treatments of heterogeneities and periodic boundary conditions for isogeometric homogenization analysis," *Int. J. Numer. Methods Eng.*, vol. 109, no. 11, pp. 1523–1548, 2017. doi: [10.1002/nme.5328](https://doi.org/10.1002/nme.5328).
- [39] R. Alberdi, G. Zhang, and K. Khandelwal, "A framework for implementation of RVE-based multiscale models in computational homogenization using isogeometric analysis," *Int. J. Numer. Methods Eng.*, vol. 114, no. 9, pp. 1018–1051, 2018. doi: [10.1002/nme.5775](https://doi.org/10.1002/nme.5775).
- [40] F. Schmidt, M. Krüger, M. -A. Keip, and C. Hesch, "Computational homogenization of higher-order continua," *Int. J. Numer. Methods Eng.*, vol. 123, no. 11, pp. 2499–2529, 2022. doi: [10.1002/nme.6948](https://doi.org/10.1002/nme.6948).
- [41] X. Du, Q. Chen, G. Chatzigeorgiou, F. Meraghni, G. Zhao and X. Chen, "Nitsche's method enhanced isogeometric homogenization of unidirectional composites with cylindrically orthotropic carbon/graphite fibers," *Compos. Sci. Technol.*, vol. 256, no. 3, 2024, Art. no. 110787. doi: [10.1016/j.compscitech.2024.110787](https://doi.org/10.1016/j.compscitech.2024.110787).
- [42] Q. Chen, X. Du, W. Wang, G. Chatzigeorgiou, F. Meraghni and G. Zhao, "Isogeometric homogenization of viscoelastic polymer composites via correspondence principle," *Compos. Struct.*, vol. 323, 2023, Art. no. 117475. doi: [10.1016/j.compstruct.2023.117475](https://doi.org/10.1016/j.compstruct.2023.117475).
- [43] C. Oskay and J. Fish, "Eigendefor-mation-based reduced order homogenization for failure analysis of heterogeneous materials," *Comput. Methods Appl. Mech. Eng.*, vol. 196, no. 7, pp. 1216–1243, 2007. doi: [10.1016/j.cma.2006.08.015](https://doi.org/10.1016/j.cma.2006.08.015).
- [44] J. Fish, *Practical Multiscale*. The Atrium, Southern Gate, Chichester, West Sussex, UK: John Wiley & Sons, 2014.
- [45] J. Fish, K. Shek, M. Pandheeradi, and M. S. Shephard, "Computational plasticity for composite structures based on mathematical homogenization: Theory and practice," *Comput. Methods Appl. Mech. Eng.*, vol. 148, no. 1-2, pp. 53–73, 1997. doi: [10.1016/S0045-7825\(97\)00030-3](https://doi.org/10.1016/S0045-7825(97)00030-3).
- [46] Z. Yuan and J. Fish, "Multiple scale eigendefor-mation-based reduced order homogenization," *Comput. Methods Appl. Mech. Eng.*, vol. 198, no. 21–26, pp. 2016–2038, 2009. doi: [10.1016/j.cma.2008.12.038](https://doi.org/10.1016/j.cma.2008.12.038).
- [47] J. Fish, Z. Yang, and Z. Yuan, "A second-order reduced asymptotic homogenization approach for nonlinear periodic heterogeneous materials," *Int. J. Numer. Methods Eng.*, vol. 119, no. 6, pp. 469–489, 2019. doi: [10.1002/nme.6058](https://doi.org/10.1002/nme.6058).
- [48] Z. Yang, Y. Liu, Y. Sun, Y. Jing, and Q. Ma, "A novel second-order reduced homogenization approach for nonlinear thermo-mechanical problems of axisymmetric structures with periodic micro-configurations," *Comput. Methods Appl. Mech. Eng.*, vol. 368, no. 3, 2020, Art. no. 113126. doi: [10.1016/j.cma.2020.113126](https://doi.org/10.1016/j.cma.2020.113126).
- [49] Z. Yang, Y. Sun, Y. Liu, and Q. Ma, "A second-order reduced multiscale approach for non-linear axisymmetric structures with periodic configurations," *Appl. Math. Model.*, vol. 88, no. 3, pp. 791–809, 2020. doi: [10.1016/j.apm.2020.07.009](https://doi.org/10.1016/j.apm.2020.07.009).
- [50] J. C. Simo and T. J. Hughes, *Computational Inelasticity*. New York, USA: Springer Science & Business Media, 2006.
- [51] G. Dvorak, *Micromechanics of Composite Materials*. New York, USA: Springer Science & Business Media, 2012.

- [52] S. V. Thiruppukuzhi and C. T. Sun, "Models for the strain-rate-dependent behavior of polymer composites," *Compos Sci. Technol.*, vol. 61, no. 1, pp. 1–12, 2001. doi: [10.1016/S0266-3538\(00\)00133-0](https://doi.org/10.1016/S0266-3538(00)00133-0).
- [53] Y. Chen, Z. Zhao, D. Li, Z. Guo, and L. Dong, "Constitutive modeling for linear viscoelastic fiber-reinforced composites," *Compos. Struct.*, vol. 263, 2021, Art. no. 113679. doi: [10.1016/j.compstruct.2021.113679](https://doi.org/10.1016/j.compstruct.2021.113679).

Appendix A

In this section, we solve the ODE equation system in Eq. (27) to obtain the matrix phase strains. With the reduced 1-index defined in Eq. (22), we can rewrite Eq. (27) into the following system of ODEs:

$$\begin{aligned} \frac{d}{dt} \begin{Bmatrix} \varepsilon_{22}^m(t) \\ \varepsilon_{33}^m(t) \end{Bmatrix} = & -\frac{1}{2} \begin{bmatrix} 1/\tau_2 + 1/\tau_3 & 1/\tau_2 - 1/\tau_3 \\ 1/\tau_2 - 1/\tau_3 & 1/\tau_2 + 1/\tau_3 \end{bmatrix} \begin{Bmatrix} \varepsilon_{22}^m(t) \\ \varepsilon_{33}^m(t) \end{Bmatrix} \\ & + \frac{1}{2} \begin{bmatrix} 1/\tau_2 + 1/\tau_3 & 1/\tau_2 - 1/\tau_3 \\ 1/\tau_2 - 1/\tau_3 & 1/\tau_2 + 1/\tau_3 \end{bmatrix} \begin{bmatrix} E_1^m & E_2^m & E_3^m \\ E_1^m & E_3^m & E_2^m \end{bmatrix} \begin{Bmatrix} \varepsilon_{11}^c(t) + \tau_1 \dot{\varepsilon}_{11}^c(t) \\ \varepsilon_{22}^c(t) + \tau_1 \dot{\varepsilon}_{22}^c(t) \\ \varepsilon_{33}^c(t) + \tau_1 \dot{\varepsilon}_{33}^c(t) \end{Bmatrix} - \begin{Bmatrix} \frac{\tau_1}{\tau_2} \psi_m P_1^m \dot{\varepsilon}_{11}^c(t) \\ \frac{\tau_1}{\tau_2} \psi_m P_1^m \dot{\varepsilon}_{11}^c(t) \end{Bmatrix} \end{aligned} \quad (A1a)$$

and

$$\frac{d\varepsilon_{23}^m(t)}{dt} = -\frac{1}{\tau_4} \varepsilon_{23}^m(t) + \frac{1}{\tau_4} E_{23}^{23,m} [\varepsilon_{23}^c(t) + \tau_1 \dot{\varepsilon}_{23}^c(t)] \quad (A1b)$$

$$\frac{d\varepsilon_{13}^m(t)}{dt} = -\frac{1}{\tau_5} \varepsilon_{13}^m(t) + \frac{1}{\tau_5} E_{13}^{13,m} [\varepsilon_{13}^c(t) + \tau_1 \dot{\varepsilon}_{13}^c(t)] \quad (A1c)$$

$$\frac{d\varepsilon_{12}^m(t)}{dt} = -\frac{1}{\tau_5} \varepsilon_{12}^m(t) + \frac{1}{\tau_5} E_{12}^{12,m} [\varepsilon_{12}^c(t) + \tau_1 \dot{\varepsilon}_{12}^c(t)] \quad (A1d)$$

with

$$\begin{aligned} \tau_2 &= \tau_1 (1 + \psi_m P_2^{mm} + \psi_m P_3^{mm}), \tau_3 = \tau_1 (1 + \psi_m P_2^{mm} - \psi_m P_3^{mm}), \\ \tau_4 &= \tau_1 (1 + \psi_m P_4^{mm}), \tau_5 = \tau_1 (1 + \psi_m P_5^{mm}) \end{aligned} \quad (A2)$$

Here $\tau_k, k = 2, 3, 4, 5$ are characteristic relaxation times for the fibrous composite materials.

For the coupled ODEs defined in Eq. (A1a), notice that

$$\frac{1}{2} \begin{bmatrix} 1/\tau_2 + 1/\tau_3 & 1/\tau_2 - 1/\tau_3 \\ 1/\tau_2 - 1/\tau_3 & 1/\tau_2 + 1/\tau_3 \end{bmatrix} = \begin{bmatrix} 1 & -1 \\ 1 & 1 \end{bmatrix} \begin{bmatrix} 1/\tau_2 & 0 \\ 0 & 1/\tau_3 \end{bmatrix} \begin{bmatrix} 1/2 & 1/2 \\ -1/2 & 1/2 \end{bmatrix} \quad (A3)$$

Define the following two strains:

$$\begin{Bmatrix} \tilde{\varepsilon}_{22}^m(t) \\ \tilde{\varepsilon}_{33}^m(t) \end{Bmatrix} = \begin{bmatrix} 1/2 & 1/2 \\ -1/2 & 1/2 \end{bmatrix} \begin{Bmatrix} \varepsilon_{22}^m(t) - E_1^m \varepsilon_{11}^c(t) - E_2^m \varepsilon_{22}^c(t) - E_3^m \varepsilon_{33}^c(t) \\ \varepsilon_{33}^m(t) - E_1^m \varepsilon_{11}^c(t) - E_3^m \varepsilon_{22}^c(t) - E_2^m \varepsilon_{33}^c(t) \end{Bmatrix} \quad (A4)$$

and the corresponding ODEs become:

$$\begin{aligned} \frac{d}{dt} \begin{Bmatrix} \tilde{\varepsilon}_{22}^m(t) \\ \tilde{\varepsilon}_{33}^m(t) \end{Bmatrix} = & - \begin{bmatrix} \frac{1}{\tau_2} & 0 \\ 0 & \frac{1}{\tau_3} \end{bmatrix} \begin{Bmatrix} \tilde{\varepsilon}_{22}^m(t) \\ \tilde{\varepsilon}_{33}^m(t) \end{Bmatrix} \\ & - \begin{bmatrix} \frac{\tau_2 - \tau_1}{\tau_2} & 0 \\ 0 & \frac{\tau_3 - \tau_1}{\tau_3} \end{bmatrix} \begin{bmatrix} 1/2 & 1/2 \\ -1/2 & 1/2 \end{bmatrix} \begin{bmatrix} E_1^m \dot{\varepsilon}_{11}^c(t) + E_2^m \dot{\varepsilon}_{22}^c(t) + E_3^m \dot{\varepsilon}_{33}^c(t) \\ E_1^m \dot{\varepsilon}_{11}^c(t) + E_3^m \dot{\varepsilon}_{22}^c(t) + E_2^m \dot{\varepsilon}_{33}^c(t) \end{bmatrix} \\ & - \begin{bmatrix} \frac{\tau_1}{\tau_2} \psi_m P_1^m \dot{\varepsilon}_{11}^c(t) \\ 0 \end{bmatrix} \end{aligned} \quad (\text{A5})$$

The solution of Eqs. (A5) can be written as

$$\tilde{\varepsilon}_{22}^m(t) = -\frac{\tau_2 - \tau_1}{\tau_2} e^{-t/\tau_2} * \left\{ \left(E_1^m + \frac{\tau_1}{\tau_2 - \tau_1} \psi_m P_1^m \right) \dot{\varepsilon}_{11}^c(t) + \frac{1}{2} (E_2^m + E_3^m) (\dot{\varepsilon}_{22}^c(t) + \dot{\varepsilon}_{33}^c(t)) \right\} \quad (\text{A6a})$$

$$\tilde{\varepsilon}_{33}^m(t) = -\frac{\tau_3 - \tau_1}{\tau_3} e^{-t/\tau_3} * \left\{ \frac{1}{2} (E_2^m - E_3^m) (-\dot{\varepsilon}_{22}^c(t) + \dot{\varepsilon}_{33}^c(t)) \right\} \quad (\text{A6b})$$

Substituting Eqs. (A6a) and (A6b) into (A4) yields the solution that

$$\begin{aligned} \varepsilon_{22}^m(t) = & E_1^m \varepsilon_{11}^c(t) + E_2^m \varepsilon_{22}^c(t) + E_3^m \varepsilon_{33}^c(t) + \tilde{\varepsilon}_{22}^m(t) - \tilde{\varepsilon}_{33}^m(t) \\ = & E_1^m \varepsilon_{11}^c(t) + E_2^m \varepsilon_{22}^c(t) + E_3^m \varepsilon_{33}^c(t) + \left[-E_1^m \frac{\tau_2 - \tau_1}{\tau_2} - \frac{\tau_1}{\tau_2} \psi_m P_1^m \right] e^{-t/\tau_2} * \dot{\varepsilon}_{11}^c(t) \\ & + \left[-\frac{1}{2} (E_2^m + E_3^m) \frac{\tau_2 - \tau_1}{\tau_2} e^{-t/\tau_2} - \frac{1}{2} (E_2^m - E_3^m) \frac{\tau_3 - \tau_1}{\tau_3} e^{-t/\tau_3} \right] * \dot{\varepsilon}_{22}^c(t) \\ & + \left[-\frac{1}{2} (E_2^m + E_3^m) \frac{\tau_2 - \tau_1}{\tau_2} e^{-t/\tau_2} + \frac{1}{2} (E_2^m - E_3^m) \frac{\tau_3 - \tau_1}{\tau_3} e^{-t/\tau_3} \right] * \dot{\varepsilon}_{33}^c(t) \end{aligned} \quad (\text{A7a})$$

$$\begin{aligned} \varepsilon_{33}^m(t) = & E_1^m \varepsilon_{11}^c(t) + E_3^m \varepsilon_{22}^c(t) + E_2^m \varepsilon_{33}^c(t) + \tilde{\varepsilon}_{22}^m(t) + \tilde{\varepsilon}_{33}^m(t) \\ = & E_1^m \varepsilon_{11}^c(t) + E_3^m \varepsilon_{22}^c(t) + E_2^m \varepsilon_{33}^c(t) + \left[-E_1^m \frac{\tau_2 - \tau_1}{\tau_2} - \frac{\tau_1}{\tau_2} \psi_m P_1^m \right] e^{-t/\tau_2} * \dot{\varepsilon}_{11}^c(t) \\ & + \left[-\frac{1}{2} (E_2^m + E_3^m) \frac{\tau_2 - \tau_1}{\tau_2} e^{-t/\tau_2} + \frac{1}{2} (E_2^m - E_3^m) \frac{\tau_3 - \tau_1}{\tau_3} e^{-t/\tau_3} \right] * \dot{\varepsilon}_{22}^c(t) \\ & + \left[-\frac{1}{2} (E_2^m + E_3^m) \frac{\tau_2 - \tau_1}{\tau_2} e^{-t/\tau_2} - \frac{1}{2} (E_2^m - E_3^m) \frac{\tau_3 - \tau_1}{\tau_3} e^{-t/\tau_3} \right] * \dot{\varepsilon}_{33}^c(t) \end{aligned} \quad (\text{A7b})$$

The shearing response Eqs. (A1b)–(A1d), can be solved similarly. Taking Eq. (A1b) as an example. Rewrite Eq. (A1b) into

$$\frac{d}{dt} \{ \varepsilon_{23}^m(t) - E_4^m \varepsilon_{23}^c(t) \} = -\frac{1}{\tau_4} \{ \varepsilon_{23}^m(t) - E_4^m \varepsilon_{23}^c(t) \} - \frac{\tau_4 - \tau_1}{\tau_4} E_4^m \dot{\varepsilon}_{23}^c(t) \quad (\text{A8})$$

so that the solution can be given by the convolution form:

$$\varepsilon_{23}^m(t) = E_4 \varepsilon_{23}^c(t) - \frac{\tau_4 - \tau_1}{\tau_4} E_4 e^{-t/\tau_4} * \dot{\varepsilon}_{23}^c(t) \quad (\text{A9a})$$

Similarly, the solutions of (A1c) and (A1d) are written with convolution form that

$$\varepsilon_{13}^m(t) = E_5 \varepsilon_{13}^c(t) - \frac{\tau_5 - \tau_1}{\tau_5} E_5 e^{-t/\tau_5} * \dot{\varepsilon}_{13}^c(t) \quad (\text{A9b})$$

$$\varepsilon_{12}^m(t) = E_5 \varepsilon_{12}^c(t) - \frac{\tau_5 - \tau_1}{\tau_5} E_5 e^{-t/\tau_5} * \dot{\varepsilon}_{12}^c(t) \quad (\text{A9c})$$

respectively.